

PRINCIPAL GEODESIC ANALYSIS IN DIRECTOR-BASED DYNAMICS OF HYBRID MECHANICAL SYSTEMS

CRISTIAN G. GEBHARDT, JENNY SCHUBERT, AND MARC C. STEINBACH

ABSTRACT. In this article, we present new computational realizations of principal geodesic analysis for the unit sphere S^2 and the special orthogonal group $SO(3)$. In particular, we address the construction of long-time smooth lifts across branches of the respective logarithm maps. To this end, we pay special attention to certain critical numerical aspects such as singularities and their consequences on the numerical precision. Moreover, we apply principal geodesic analysis to investigate the behavior of several mechanical systems that are very rich in dynamics. The examples chosen are computationally modeled by employing a director-based formulation for rigid and flexible mechanical systems. Such a formulation allows to investigate our algorithms in a direct manner while avoiding the introduction of additional sources of error that are unrelated to principal geodesic analysis. Finally, we test our numerical machinery with the examples and, at the same time, we gain deeper insight into their dynamical behavior.

1. INTRODUCTION

The motion of rigid and flexible mechanical systems is inherently nonlinear and very rich in geometric structure. Although the mathematical theory behind the description of motion is well known, understanding this geometric structure is by no means trivial. In general, motion can be understood abstractly as a path on some manifold, regardless of whether it is obtained as the solution of a set of equations or whether it is observed or measured from a real system. Moreover, some peculiarities or some patterns can be as well identified or recognized from it. Thus, having such an understanding is fundamental to interpret the language of the motion. However, we still need to further develop our mathematical tools to decode such a language. One possible strategy to accomplish this challenging task is to employ principal geodesic analysis (PGA), which generalizes principal component analysis (PCA) from Euclidean spaces to nonlinear Riemannian manifolds [16, 20]. Even though the basic ideas behind PGA are mathematically well founded and established in the community, exact details depend very much on the particular manifold under consideration, and technical requirements may depend on the application context. In general there are many ways to develop a computational realization that is sufficiently generic, performant, robust, and accurate. Moreover, some of these areas still remain either relatively unexplored or not investigated. This is the primary reason why this field of research has attracted much attention in recent years.

As follows, we indicate some of the most important contributions to PGA made in the last two decades. Fletcher et al. [5] carry out statistics of shape for medical image processing and recognize that medial descriptions are in fact elements of a Lie group, while Fletcher et al. [6] introduce PGA for the nonlinear statistics of shape based upon the previous findings. In [22] the exact computation of the PGA of data on the rotation group $SO(3)$ is presented. Relying on PGA, Tournier et al. [26] develop a lossy compression method for human motion data. Huckemann et al. [15] introduce a general framework

Date: September 9, 2022.

2020 Mathematics Subject Classification. 65D15, 70K99, 74H40, 74K10, 74K25.

Key words and phrases. Principal geodesic analysis, unit sphere S^2 , special orthogonal group $SO(3)$, singularities and numerical precision, director-based dynamics of mechanical systems.

for PCA on quotient spaces that result from an isometric Lie group action on a complete Riemannian manifold. Fotouhi and Golalizadeh [7] investigate the DNA (deoxyribonucleic acid) molecular structure by means of PGA. Ren et al. [21] employ PGA to construct classifiers for embedded non-Euclidean data. In [25] methods are developed to numerically solve optimization problems over spaces of geodesics, where PGA represents an important application of such an optimization strategy. Salehian et al. [23] present an incremental version of PGA with applications to movement disorder classification. Chakraborty et al. [3] present an efficient exact-PGA algorithm for constant curvature manifolds. In [19] Taylor expansions are obtained for PGA, which lead to closed-form approximations while revealing the impact of scale, curvature, and the distribution of data on PGA and on the corresponding tangent space approximations. Sittel et al. [24] specialize PGA to the torus in the context of protein dynamics. In [13] an invariant PGA in the space of discrete shells is proposed and applied to model-constrained mesh editing and to reconstruction of dense animated meshes from sparse motion capture markers. Cazelles et al. [2] consider the analysis of datasets whose elements are random histograms and provide a detailed comparison of PGA versus log-PCA in the Wasserstein space. Gebhardt et al. [11] present a PGA framework to analyze the nonlinear dynamics of beam structures. Curry et al. [4] develop a PGA specialization based on nested sequences of totally geodesic submanifolds of symmetric spaces. And recently, Hernandez [14] investigates the efficient computation of diffeomorphisms belonging to geodesics using PGA in spaces of diffeomorphisms.

In this article, we present new computational realizations of PGA for the unit sphere S^2 and the special orthogonal group $SO(3)$. In particular, we address the construction of long-time smooth lifts across branches of the respective logarithm maps. This requires paying special attention to certain critical numerical aspects that have not been addressed extensively in the literature, such as singularities (which arise due to the compactness and rotational symmetry of the two manifolds) and their consequences on the numerical precision. Moreover, we apply PGA to investigate the dynamic behavior of several mechanical systems: a swinging rubber rod, a free-oscillating cantilever beam, a flexible triple pendulum, a horizontal-axis wind turbine, a tumbling cylinder, a free-flying plate, and a shell pendulum. To this end, the examples are computationally modeled by employing a director-based formulation for rigid and flexible mechanical systems previously developed by one of the authors [9, 8, 10]. Such a director-based formulation provides a natural description of motion in terms of product manifolds of S^2 or $SO(3)$ and thus, the application of our PGA realization is direct and straightforward. Although more standard mechanical formulations can also be considered, these would require further numerical pre- and post-processing of the solution. Such additional steps would introduce, of course, further sources of error that are not related, in any form, to PGA. Moreover, these errors are even not segregable for our accuracy analysis and therefore, we refrain from considering those director-free formulations. At any rate, the choice of the examples listed before is by no means arbitrary. On the one hand, the examples chosen exhibit very rich dynamics while enabling us to deeply test the numerical machinery of our PGA realization. On the other hand, applying PGA to these examples allows us to gain deeper insight in their dynamic behavior. Gaining such a deeper insight is not possible with standard linear methods such as modal analysis or PCA due to the fact that these systematically destroy the underlying geometric structure of the motion. Thus, the current work provides a very robust approach to improve the understanding of the subject. This approach has as well the potential to be used for deriving data-driven reduced-order models that are truly structure-preserving. However, such a derivation of reduced-order models falls outside the scope of the current manuscript and will therefore be addressed in future work.

The present work is organized as follows: In Section 2, we briefly introduce the underlying mechanical setting relying on a director-based kinematical description. Herein we present the *canonical models* together with their numerical treatment, i.e., discretization

in space and time. In Section 3, we succinctly outline the theory behind PGA. Then, we consider the unit sphere S^2 as well as the special orthogonal group $SO(3)$, which are two manifolds that play a fundamental role in classical mechanics. In Section 4, we describe the numerical implementation of PGA for the two manifolds of interest and carry out statistics to characterize the accuracy that can be achieved. In Section 5, we carry out numerical investigations by considering the mechanical systems mentioned above. Finally, Section 6 is devoted to conclusions, limitations and possible future work.

2. DIRECTOR-BASED DYNAMICS

To describe the dynamic behavior of a holonomically constrained mechanical system, we need to consider: *i*) a base manifold Q (often a Euclidian space) of dimension s with a *configuration map* $q: \bar{\Omega} \times [0, T] \rightarrow Q$ where $\bar{\Omega} \subset \mathbb{R}^d$ for $d \in \{1, 2, 3\}$ is open and bounded with Lipschitz boundary; and, *ii*) a *constraint map* $h: Q \rightarrow \mathbb{R}^m$ such that $h(q(\theta, t))$ vanishes identically for $(\theta, t) \in \bar{\Omega} \times [0, T]$. Then, $Q^h := \{q \in Q: h(q) = 0\}$ defines the submanifold of Q on which the actual dynamics of the mechanical system is going to take place. Note that we prefer to work on Q rather than describing the system by means of a minimal representation, i.e., working directly on the *configuration manifold* Q^h , since this usually allows for a more convenient and efficient numerical formulation. Due to practical reasons, we adopt a variational formulation of the dynamics based on the least action principle, which holds for almost every $t \in [0, T]$:

$$\int_{\bar{\Omega}} (\langle \delta q, \mathcal{M}(q) \nabla_{\dot{q}}(\dot{q}) + f^{\text{int}}(q, S) - f^{\text{ext}} + \mathcal{H}(q)^T \lambda \rangle + \langle \delta \lambda, h(q) \rangle) d\theta = 0. \quad (1)$$

For this, we also need to consider the linear image space Λ of the Lagrange multipliers $\lambda: \bar{\Omega} \times [0, T] \rightarrow \Lambda$. Then, δq and $\delta \lambda$ are admissible variations of q and λ , respectively, hence $\delta q(\theta) \in T_{q(\theta, t)}Q$ and $\delta \lambda(\theta) \in T_{\lambda(\theta, t)}\Lambda \cong \Lambda$. Moreover, $\mathcal{M}(q)$ is a symmetric, bounded and nonnegative mass operator. It is the metric tensor on Q^h , induced by the kinetic energy functional

$$\frac{1}{2} \int_{\bar{\Omega}} \rho \langle \dot{x}, \dot{x} \rangle d\theta = \frac{1}{2} \|\dot{q}\|_{\mathcal{M}(q)}^2, \quad (2)$$

where $\rho(\theta)$ is the mass density per unit of volume. Moreover, $x(\theta, t) \in \mathbb{R}^3$ is the position of $q(\theta, t)$ in an inertial coordinate system, and $\nabla_{\dot{q}}(\dot{q})$ denotes the covariant derivative of the velocity field along itself, which for a constant mass operator reduces to the second time derivative of the configuration, namely $\nabla_{\dot{q}}(\dot{q}) = \ddot{q}$. The internal force covector field f^{int} is implicitly defined through the identity

$$\int_{\bar{\Omega}} \langle \delta q, f^{\text{int}}(q, S) \rangle d\theta = \int_{\bar{\Omega}} \langle \delta E(q), S \rangle d\theta,$$

where $E(q)$ is a suitable strain measure, i.e., invariant under affine transformations, S is the concomitant stress measure, and $\langle \delta E(q), S \rangle$ denotes the Euclidian scalar product (if (E, S) are represented as vectors) or the Frobenius scalar product $\text{Tr}(\delta E(q)^T S)$ (if they are represented as matrices). The pair (E, S) depends on the specific mechanical model under consideration. Later on, we are going to introduce three mechanical models, namely the rigid body, the geometrically exact beam, and the geometrically exact shell. At any rate, the former identity establishes that the virtual work done by internal forces is identical to the work done by internal stresses, where the stress measure is given by

$$S = \partial_E W^{\text{int}}(E)$$

for W^{int} representing an internal elastic energy functional. Without loss of generality, the external force covector field f^{ext} is assumed to be only a function of time and bounded. The operator $\mathcal{H}(q) \in L(T_q Q, \mathbb{R}^m)$ is the derivative of $h(q)$ and is assumed to be bounded and surjective. At this point, it is worthwhile to point out that we are going to assume that $\mathcal{M}(q)$ is positive definite on the subspace $\ker(\mathcal{H}(q)) \subseteq T_q Q$, which together with the

condition $\ker(\mathcal{M}(q)) \cap \ker(\mathcal{K}(q)) = \{0\}$, for $\mathcal{K}(q) \in L(T_q Q, T_q Q^*)$ being the bounded and nonnegative operator associated to the bilinear form

$$(\delta q_1, \delta q_2) \mapsto \partial_E^2 \mathcal{W}^{\text{int}}(E(q))(\partial_q E(q)\delta q_1, \partial_q E(q)\delta q_2),$$

provides necessary and sufficient conditions for well-posedness of the problem in its local form. It should be noticed that nonnegativity, boundedness, and surjectivity occur in the appropriate spaces, which are certainly model specific.

Before presenting the mechanical models, we define the two manifolds that are of special interest for our present analysis. The first one is the Euclidian 2-sphere

$$S^2 := \{d \in \mathbb{R}^3: \|d\|_2 = 1\},$$

where d is normally called a *director*. The second one is the special orthogonal group

$$SO(3) := \{R \in \mathbb{R}^{3 \times 3}: R^T R = I, \det(R) = 1\},$$

where R is the *rotation tensor*. A rotation tensor can be built from three directors as

$$R = d_1 \otimes e^1 + d_2 \otimes e^2 + d_3 \otimes e^3,$$

with $\{e^1, e^2, e^3\}$ standing for the covariant basis associated to any given orthonormal basis $\{e_1, e_2, e_3\}$ while providing that the directors' orthogonality conditions hold, namely

$$\langle d_1, d_2 \rangle = \langle d_2, d_3 \rangle = \langle d_3, d_1 \rangle = 0.$$

These basic definitions are succinctly presented with the purpose of placing the current ideas in an adequate setting. However, further mathematical details on these two manifolds and some interesting numerical properties are investigated in the coming sections.

In the context of nonlinear dynamics, there are basically three *canonical models* that attract in particular our attention. These rely then on configuration manifolds that differ from the trivial one, namely the three-dimensional Euclidean space. Below, we are going to introduce them briefly. For sake of brevity, we assume that the greek indices α and β can take values $\{1, 2\}$ and the latin indices i and j can take values $\{1, 2, 3\}$. It is of special convenience in this section to adopt as well the repeated-index convention. We also use the subscript $(\cdot)_0$ when we have adopted a specific reference, such as L_0 , S_0 , or Ω_0 for initial length, initial surface, or initial volume, correspondingly, or a reference point for the rigid body, the center line for the beam, or the mean surface for the shell, respectively.

The *first canonical model* is the rigid body, whose configuration manifold Q_{rb}^h is $\mathbb{R}^3 \times SO(3)$ of dimension six in $Q_{\text{rb}} = \mathbb{R}^3 \times \mathbb{R}^{3 \times 3}$ of dimension 12, with configuration map $q_{\text{rb}} : [0, T] \rightarrow Q_{\text{rb}}$. For representing $SO(3)$, we use three directors $d_i(t)$ constrained to remain orthonormal at any time. Then the configuration, position, and constraint maps, with $\Omega_{\text{rb}} \subset \mathbb{R}^3$ the set of all points belonging to the rigid body and $\theta \in \Omega_{\text{rb}}$, are given as

$$\begin{aligned} q_{\text{rb}}(t) &= (x_0(t), d_1(t), d_2(t), d_3(t)) \in Q_{\text{rb}} \cong \mathbb{R}^{12}, \\ x_{\text{rb}}(\theta, t) &= x_0(t) + \theta^1 d_1(t) + \theta^2 d_2(t) + \theta^3 d_3(t) \in \mathbb{R}^3, \\ h_{\text{rb}}(x_0, d_1, d_2, d_3) &= (\{\|d_i\|_2^2 - 1\}_{i=1}^3, \langle d_1, d_2 \rangle, \langle d_2, d_3 \rangle, \langle d_3, d_1 \rangle) \in \mathbb{R}^6. \end{aligned}$$

As its name indicates, a rigid body is infinitely stiff and therefore, its internal potential energy functional is the trivial one, namely

$$\mathcal{W}_{\text{rb}}^{\text{int}} = 0.$$

Clearly, the chosen setting is not minimal at all. However, this leads to mass operators that are constant and thus, it turns out to be very convenient from the numerical point of view. The resulting functions are (multivariate) polynomials of order two, due to the presence of the orthonormality constraints.

The *second canonical model* is the geometrically exact beam, whose configuration manifold Q_{geb}^h is again $\mathbb{R}^3 \times SO(3)$, with configuration map $q_{\text{geb}} : [0, L_0] \times [0, T] \rightarrow Q_{\text{geb}} = Q_{\text{rb}}$.

Any point belonging to the geometrically exact beam is represented by the cross-sectional coordinates $(\theta^1, \theta^2) \in A_0$ and the length coordinate $\theta^3 \in [0, L_0]$ as

$$\begin{aligned} \mathbf{q}_{\text{geb}}(\theta^3, \mathbf{t}) &= (\mathbf{x}_0(\theta^3, \mathbf{t}), \mathbf{d}_1(\theta^3, \mathbf{t}), \mathbf{d}_2(\theta^3, \mathbf{t}), \mathbf{d}_3(\theta^3, \mathbf{t})) \in Q_{\text{geb}} \cong \mathbb{R}^{12}, \\ \mathbf{x}_{\text{geb}}(\theta, \mathbf{t}) &= \mathbf{x}_0(\theta^3, \mathbf{t}) + \theta^1 \mathbf{d}_1(\theta^3, \mathbf{t}) + \theta^2 \mathbf{d}_2(\theta^3, \mathbf{t}) \in \mathbb{R}^3, \\ h_{\text{geb}}(\mathbf{x}_0, \mathbf{d}_1, \mathbf{d}_2, \mathbf{d}_3) &= h_{\text{rb}}(\mathbf{x}_0, \mathbf{d}_1, \mathbf{d}_2, \mathbf{d}_3) \in \mathbb{R}^6. \end{aligned}$$

Even provided that a two-director formulation is possible, we choose a three-director formulation, which again strongly simplifies the complexity of the governing equations. In contrast to the rigid body, we can indeed define model-specific deformation measures such as the axial and shear strains as

$$\Gamma^i := \langle \partial_{\theta^3} \mathbf{x}_0, \mathbf{d}_i \rangle - \Gamma_0^i,$$

as well as the bending and torsional strains as

$$\mathbf{K}^i := \frac{1}{2} \varepsilon_{j k}^i (\langle \partial_{\theta^3} \mathbf{d}_j, \mathbf{d}_k \rangle - \langle \partial_{\theta^3} \mathbf{d}_k, \mathbf{d}_j \rangle) - \mathbf{K}_0^i.$$

The internal elastic energy functional per unit of length arises after integrating over the cross section and then, we have the specialization

$$\int_{\Omega_0} W^{\text{int}}(\mathbf{E}) \, d\theta \rightsquigarrow \int_0^{L_0} W_{\text{geb}}^{\text{int}}(\Gamma, \mathbf{K}) \, d\ell.$$

From this, internal resultants per unit of length can be defined as

$$\mathbf{N}_{\text{geb}} = \partial_{\Gamma} W_{\text{geb}}^{\text{int}}(\Gamma, \mathbf{K}) \quad \text{and} \quad \mathbf{M}_{\text{geb}} = \partial_{\mathbf{K}} W_{\text{geb}}^{\text{int}}(\Gamma, \mathbf{K}),$$

respectively, and the components of the internal force covector field $f_{\text{geb}}^{\text{int}}$ become

$$(f_{\text{geb}}^{\text{int}}(\mathbf{q}, \mathbf{N}_{\text{geb}}, \mathbf{M}_{\text{geb}}))_{\alpha} = (\partial_{\mathbf{q}} \Gamma)_{\alpha}^i (\mathbf{N}_{\text{geb}})_i + (\partial_{\mathbf{q}} \mathbf{K})_{\alpha}^i (\mathbf{M}_{\text{geb}})_i.$$

The *third canonical model* is the geometrically exact shell, whose configuration manifold Q_{ges}^h is $\mathbb{R}^3 \times S^2$ of dimension five in $Q_{\text{ges}} = \mathbb{R}^3 \times \mathbb{R}^3$ of dimension six, with configuration map $\mathbf{q}_{\text{ges}} = (\mathbf{x}_0, \mathbf{d}_3): S_0 \times [0, T] \rightarrow Q_{\text{ges}}$. Any point across the geometrically exact shell is represented by $\theta^3 \in [-\frac{1}{2}H_0, \frac{1}{2}H_0]$ (with H_0 standing for the thickness) at the surface coordinates $(\theta^1, \theta^2) \in S_0$ and is described by

$$\begin{aligned} \mathbf{q}_{\text{ges}}(\theta^1, \theta^2, \mathbf{t}) &= (\mathbf{x}_0(\theta^1, \theta^2, \mathbf{t}), \mathbf{d}_3(\theta^1, \theta^2, \mathbf{t})) \in Q_{\text{ges}} \cong \mathbb{R}^6, \\ \mathbf{x}_{\text{ges}}(\theta, \mathbf{t}) &= \mathbf{x}_0(\theta^1, \theta^2, \mathbf{t}) + \theta^3 \mathbf{d}_3(\theta^1, \theta^2, \mathbf{t}) \in \mathbb{R}^3, \\ h_{\text{ges}}(\mathbf{x}_0, \mathbf{d}_3) &= \|\mathbf{d}_3\|_2^2 - 1 \in \mathbb{R}^1. \end{aligned}$$

Again we can define model-specific deformation measures such as the membrane strains,

$$\epsilon^{\alpha\beta} := \langle \partial_{\theta^{\alpha}} \mathbf{x}_0, \partial_{\theta^{\beta}} \mathbf{x}_0 \rangle - \epsilon_0^{\alpha\beta},$$

the bending strains,

$$\kappa^{\alpha\beta} := \langle \partial_{\theta^{\alpha}} \mathbf{x}_0, \partial_{\theta^{\beta}} \mathbf{d}_3 \rangle + \langle \partial_{\theta^{\beta}} \mathbf{x}_0, \partial_{\theta^{\alpha}} \mathbf{d}_3 \rangle - \kappa_0^{\alpha\beta},$$

and the transverse shear strains,

$$\gamma^{\alpha} := \langle \partial_{\theta^{\alpha}} \mathbf{x}_0, \mathbf{d}_3 \rangle - \gamma_0^{\alpha}.$$

To avoid confusion of the model-specific measures with those corresponding to the geometrically exact beam, we use small fonts. However, for the reader with experience in continuum mechanics this would result to be a small modification with respect to the standard notation, where small fonts are used for the spatial description while large fonts are used for the material description. The internal elastic energy functional per unit of surface arises after integrating across the thickness and then, we have the specialization

$$\int_{\Omega_0} W^{\text{int}}(\mathbf{E}) \, d\theta \rightsquigarrow \int_{S_0} W_{\text{ges}}^{\text{int}}(\epsilon, \kappa, \gamma) \, dS.$$

From this, internal resultants per unit of surface can be defined as

$$N_{\text{ges}} = \partial_\epsilon W_{\text{ges}}^{\text{int}}(\epsilon, \gamma, \kappa), \quad M_{\text{ges}} = \partial_\kappa W_{\text{ges}}^{\text{int}}(\epsilon, \gamma, \kappa), \quad F_{\text{ges}} = \partial_\gamma W_{\text{ges}}^{\text{int}}(\epsilon, \gamma, \kappa),$$

respectively, and the components of the internal force covector field $f_{\text{ges}}^{\text{int}}$ become

$$(f_{\text{ges}}^{\text{int}}(q, N_{\text{ges}}, M_{\text{ges}}, F_{\text{ges}}))_\alpha = (\partial_q \epsilon)_\alpha^{\alpha\beta} (N_{\text{ges}})_{\alpha\beta} + (\partial_q \kappa)_\alpha^{\alpha\beta} (M_{\text{ges}})_{\alpha\beta} + (\partial_q \gamma)_\alpha^\alpha (F_{\text{ges}})_\alpha.$$

2.1. Spatial and Temporal Discretizations. Here we consider the spatial discretization by means of the finite element method and then proceed with the temporal discretization which is designed for structure-preserving integration.

A finite element in \mathbb{R}^d is a triplet (K, P, Σ) where: *i*) K is a non-empty closed and bounded subset of \mathbb{R}^d with Lipschitz boundary; *ii*) P is a finite-dimensional vector space of functions on K ; and, *iii*) Σ is a set of linear forms $\{\sigma_i\}_{i \in \mathcal{N}}$, with $\mathcal{N} := \{1, \dots, n\}$, that are P -unisolvant and known as degrees of freedom. In addition there is a basis $\{\phi_i\}_{i \in \mathcal{N}}$ for P such that $\sigma_i(\phi_j) = \delta_{ij}$ for any $i, j \in \mathcal{N}$, where the functions ϕ_i are known as shape functions. Let the triplet (K, P, Σ) be a scalar-valued finite element; if there is a set of points $\{\theta_i\}_{i \in \mathcal{N}}$ in K where $\sigma_i(p) = p(\theta_i)$ for any $p \in P$, the finite element is known as Lagrange finite element and the points are known as nodes. Then, the property $\phi_i(\theta_j) = \delta_{ij}$ holds for any $i, j \in \mathcal{N}$. The extension to vector-valued Lagrange finite elements is carried out simply by considering all components simultaneously.

Our spatial mesh \mathcal{T}_h is then a set of compact elements $\{K_i\}_{i \in \mathcal{N}_e}$, with $\mathcal{N}_e := \{1, \dots, N_e\}$ where N_e is the number of elements, such that

$$\bar{\Omega} = \bigcup_{i \in \mathcal{N}_e} K_i, \quad \text{int}(K_i) \cap \text{int}(K_j) = \emptyset \text{ if } i \neq j, \quad \partial\Omega \subset \bigcup_{i \in \mathcal{N}_e} \partial K_i.$$

Let $V(K)$ be a Sobolev space associated to the element K and $J_K: V(K) \rightarrow P$ be a local interpolation operator defined by

$$J_K(v) = \sum_{i \in \mathcal{N}} \sigma_i(v) \phi_i, \quad v \in V(K),$$

for Lagrange finite elements and $P = \mathbb{P}^k(K)$ containing the polynomials of degree up to k . Then the following estimate holds

$$\|v - J_K(v)\|_{L^2(K)} \leq c h_K^{\ell+1} \|v\|_{H^{\ell+1}(K)}, \quad v \in V(K), \quad \ell \leq k,$$

with c being a constant, h_K representing the diameter of the largest ball contained in K , and all partial derivatives assumed in the weak sense. The estimate can be extended to all of Ω as follows:

$$\|v - J_h(v)\|_{L^2(\Omega)} \leq c h^{\ell+1} \|v\|_{H^{\ell+1}(\Omega)}, \quad v \in V, \quad \ell \leq k,$$

where J_h is the global interpolation operator, h is the largest h_K in the mesh \mathcal{T}_h and V is the space in which the variational problem is formulated. For flexible mechanical models considered in this work we need to consider

$$V := H^1(\Omega)^s,$$

the continuous space equipped with s coordinate fields q_i in which the problem is stated, and

$$V_h := \{v_h \in C^0(\Omega)^s \cap V: v_h|_{K_i} \in \mathbb{P}^1(K_i) \forall i \in \mathcal{N}_e\},$$

the discrete space in which the problem is approximated. Thus, V_h is a subspace of V .

Particularly for our two flexible models, the geometrically exact beam and geometrically exact shell, we have

$$q_{\text{geb}}(\theta^3; t) \approx q_{\text{geb},h}(\theta^3; t) = \sum_{i \in \mathcal{N}_e} \Phi_{\text{geb},i}(\theta^3) \hat{q}_{\text{geb},i}(t) \quad (s = 12)$$

and

$$\mathbf{q}_{\text{ges}}(\theta^1, \theta^2; \mathbf{t}) \approx \mathbf{q}_{\text{ges,h}}(\theta^1, \theta^2; \mathbf{t}) = \sum_{i \in \mathcal{N}_e} \Phi_{\text{ges},i}(\theta^1, \theta^2) \hat{\mathbf{q}}_{\text{ges},i}(\mathbf{t}) \quad (s = 6),$$

where Φ_i is a matrix containing all shape functions and $\hat{\mathbf{q}}_i$ is the set of nodal degrees of freedom. The two-node beam element has twelve coordinate fields per node, one position vector and three directors, $\hat{\mathbf{q}} = (x_{0,i}, d_{1,i}, d_{2,i}, d_{3,i})_{i=1}^2$, whereas the four-node shell element has six coordinate fields per node, one position vector and one director, $\hat{\mathbf{q}} = (x_{0,i}, d_{3,i})_{i=1}^4$. To complete the description, we enforce the constraints associated to the directors only at the nodal level. Then we can proceed with approximations for all the terms present in (1) as

$$\begin{aligned} \int_{\Omega} \langle \delta \mathbf{q}_h, \mathcal{M}(\mathbf{q}_h) \nabla_{\hat{\mathbf{q}}_h}(\dot{\mathbf{q}}_h) \rangle d\theta &= \left\langle \delta \hat{\mathbf{q}}, \int_{\Omega} \hat{\mathcal{M}}(\hat{\mathbf{q}}) \hat{\nabla}_{\hat{\mathbf{q}}}(\dot{\hat{\mathbf{q}}}) d\theta \right\rangle, \\ \int_{\Omega} \langle \delta \mathbf{q}_h, \mathbf{f}^{\text{int}}(\mathbf{q}_h) - \mathbf{f}^{\text{ext}} \rangle d\theta &= \left\langle \delta \hat{\mathbf{q}}, \int_{\Omega} (\hat{\mathbf{f}}^{\text{int}}(\hat{\mathbf{q}}) - \hat{\mathbf{f}}^{\text{ext}}) d\theta \right\rangle, \\ \int_{\Omega} \langle \delta \mathbf{q}_h, \mathcal{H}(\mathbf{q}_h)^T \lambda_h \rangle d\theta &= \langle \delta \hat{\mathbf{q}}, \hat{\mathcal{H}}(\hat{\mathbf{q}})^T \hat{\lambda} \rangle, \\ \int_{\Omega} \langle \delta \lambda_h, \mathbf{h}(\mathbf{q}_h) \rangle d\theta &= \langle \delta \hat{\lambda}, \hat{\mathbf{h}}(\hat{\mathbf{q}}) \rangle. \end{aligned}$$

It is worthwhile to mention that upon linearization, removing of rigid body motions from \mathbf{V} and \mathbf{V}_h , and turning off the term corresponding to the time derivative of the momentum, the convergence rate

$$\|\mathbf{q} - \mathbf{q}_h\|_{L^2(\Omega)} \leq c h^2$$

can be derived. Even provided that this rate does not necessarily hold for the nonlinear setting, numerical experiments suggest that the nonlinear problem may also exhibit optimal convergence behavior.

To implicitly integrate the system's dynamics in time, we are going to rely on a discrete version of the balance equation at time instant $t_{n+\frac{1}{2}}$. Moreover, the time grid is uniform and characterized by the fixed time step Δt . Since the problem is already discretized in space, we assume that all quantities are finite-dimensional or nodal quantities and therefore drop $(\hat{\cdot})$ from our notation. To properly set up the numerical integration scheme, we employ second-order approximations for the position and the velocity,

$$\mathbf{q}_{n+\frac{1}{2}} \approx \frac{\mathbf{q}_n + \mathbf{q}_{n+1}}{2} \quad \text{and} \quad \dot{\mathbf{q}}_{n+\frac{1}{2}} \approx \frac{\mathbf{q}_{n+1} - \mathbf{q}_n}{\Delta t},$$

for the time derivative of the momentum,

$$(\mathcal{M}(\mathbf{q}) \nabla_{\dot{\mathbf{q}}})_{n+\frac{1}{2}} \approx \frac{\mathcal{M}(\mathbf{q}_{n+1}) \dot{\mathbf{q}}_{n+1} - \mathcal{M}(\mathbf{q}_n) \dot{\mathbf{q}}_n}{\Delta t} - \frac{1}{2} \partial_{\xi} \langle \dot{\mathbf{q}}_{n+\frac{1}{2}}, \mathcal{M}(\xi) \dot{\mathbf{q}}_{n+\frac{1}{2}} \rangle \Big|_{\xi=\mathbf{q}_{n+\frac{1}{2}}},$$

and for the internal force covector field,

$$(\mathbf{f}^{\text{int}}(\mathbf{q}))_{n+\frac{1}{2}} \approx \frac{1}{2} \int_{-1}^{+1} (\partial_{\mathbf{q}} \mathbf{E})_{n+\frac{1}{2}} \cdot \mathbf{S}(\mathbf{q}(\xi)) d\xi$$

(where “ \cdot ” denotes the contraction of a $(m, n+1)$ -tensor with a (n, m) -tensor resulting in a one-form [12]) with

$$\mathbf{q}(\xi) := \frac{1}{2}(1 - \xi)\mathbf{q}_n + \frac{1}{2}(1 + \xi)\mathbf{q}_{n+1}$$

and

$$(\partial_{\mathbf{q}} \mathbf{E})_{n+\frac{1}{2}} = \partial_{\mathbf{q}} \mathbf{E}(\mathbf{q}_{n+\frac{1}{2}}).$$

In addition, the constraint force is approximated as

$$(\mathcal{H}(q)^\top \lambda)_{n+\frac{1}{2}} \approx \frac{1}{2} \int_{-1}^{+1} \mathcal{H}(q(\xi))^\top \lambda_{n+\frac{1}{2}} d\xi$$

while the constraint equation is enforced at time instant t_{n+1} , i.e. $h(q_{n+1}) = 0$.

The integration scheme then proceeds as follows: *i*) q_n and \dot{q}_n are given and thus, used to initially estimate q_{n+1} and \dot{q}_{n+1} ; *ii*) from the balance equation at time instant $t_{n+\frac{1}{2}}$ and the constraint equation at time instant t_{n+1} , q_{n+1} and $\lambda_{n+\frac{1}{2}}$ are to be found, up to a tolerance ε , through an iterative procedure such as Newton's method; and, *iii*) \dot{q}_{n+1} is finally calculated with the formula $\frac{2}{\Delta t}(q_{n+1} - q_n) - \dot{q}_n$.

This hybrid numerical strategy, beyond being second-order accurate, identically preserves linear and angular momentum as well as total energy. Therefore, this turns out to be good enough for our purpose.

3. THEORETICAL BACKGROUND OF PGA

PGA consists of three steps: *i*) lifting a discrete trajectory from the manifold to a suitable tangent space by means of *logarithm maps*; *ii*) performing a PCA in that tangent space; and *iii*) mapping the results back to the manifold by an *exponential map*. This section provides the mathematical notation, concepts, and facts that we need to formulate steps *i*) and *iii*) for the manifolds of interest and to understand certain difficulties caused by singularities. The presentation is essentially rigorous but we avoid unnecessary abstraction, technical details, and proofs.

3.1. Riemannian Manifolds. Before turning to the manifolds of interest, we give a brief introduction into the general theory. Background material can be found in any textbook on Riemannian geometry, such as [18]. For the purpose of this paper, a (*smooth*) *manifold* M of dimension m is a subset of \mathbb{R}^n defined by a smooth surjective map $F: \mathbb{R}^n \rightarrow \mathbb{R}^{n-m}$,

$$M := \{x \in \mathbb{R}^n: F(x) = 0\}, \quad \text{rank } F'(x) = n - m \quad \forall x \in M.$$

Of course, \mathbb{R}^n is itself a manifold (set $F := 0$). One of the simplest nontrivial examples is the $(n - 1)$ -dimensional manifold of unit vectors (or *directors*) in \mathbb{R}^n : the unit sphere

$$S^{n-1} := \{d \in \mathbb{R}^n: \|d\|_2^2 - 1 = \langle d, d \rangle - 1 = 0\}.$$

Every point x on a manifold M has an attached *tangent space* $T_x M \subset M \times \mathbb{R}^n$ defined as

$$T_x M := \{(x, v) \in \{x\} \times \mathbb{R}^n: F'(x)v = 0\} = \{x\} \times \{v: F'(x)v = 0\},$$

which is a *linear* space isomorphic to \mathbb{R}^m . If I is an interval and $c: I \rightarrow M$ a smooth curve, then $\dot{c}(t)$ is a tangent vector in $T_{c(t)} M$ for each $t \in I$. Moreover, the tangent space $T_x M$ depends smoothly on x so that \dot{c} is a smooth curve in the set of all tangent spaces, called the *tangent bundle* TM of M , which is also a manifold (of dimension $2m$ in \mathbb{R}^{2n}),

$$TM := \{(x, v) \in \mathbb{R}^n \times \mathbb{R}^n: (F(x), F'(x)v) = 0\}.$$

In case of the $(n - 1)$ -sphere, for instance, the tangent space at d is essentially the space $\{d\}^\perp$ of vectors that are orthogonal to d ,

$$T_d S^{n-1} = \{d\} \times \{v \in \mathbb{R}^n: \langle d, v \rangle = 0\} = \{d\} \times \{d\}^\perp.$$

Now a *Riemannian metric* on M is intuitively a set of scalar products, one on each tangent space $T_x M$, that vary smoothly with $x \in M$. Formally it is a smooth map g from M into a subset of the *tensor bundle* $S^2 M$ of symmetric bilinear forms on $T_x M$, which has a definition similar to the bundle TM and is again a manifold. Note that every scalar product on \mathbb{R}^n is a Riemannian metric that does not depend on x and that *induces* such a metric on M : $g(x)(v, w) = \langle v, w \rangle$ for $v, w \in \mathbb{R}^n$ or $v, w \in T_x M$. With a Riemannian metric, M becomes a *Riemannian manifold* and we can generalize the notion of straight lines in \mathbb{R}^n to *geodesics* on M , which are solutions of a certain second order differential equation

that is entirely determined by the metric g . Every geodesic $c: I \rightarrow M$ has constant speed $s = g(c(t))(\dot{c}(t), \dot{c}(t))^{1/2}$, and it is the unique shortest curve between sufficiently close points $x_1 = c(t_1)$, $x_2 = c(t_2)$, thus defining $d_M(x_1, x_2) := s|t_1 - t_2|$ as their *distance* in M . Considering S^{n-1} again, we take the scalar product on \mathbb{R}^n as Riemannian metric g . Then every geodesic $c: \mathbb{R} \rightarrow S^{n-1}$ has the form $c(t) = \cos(st)d + \sin(st)e$, where d, e are orthogonal vectors in S^{n-1} and $s \geq 0$ is the speed. If $s > 0$, c wraps around S^{n-1} on a circular orbit.

We are now ready to address the key concepts for PGA. To define the exponential map, we use the unique geodesic c_v that has a given vector $v \in T_x M$ as initial tangent:

$$\exp_x: \mathcal{U}_x \subseteq T_x M \rightarrow M, \quad \exp_x(v) := c_v(1) \quad \text{where} \quad \dot{c}_v(0) = v.$$

Clearly, $\exp_x(0) = x$, and by the Picard–Lindelöf theorem \exp_x is defined on some open neighborhood \mathcal{U}_x of 0. On our manifolds of interest it is defined globally and is actually a surjective map. In particular, for $\exp_d: T_d S^{n-1} \rightarrow S^{n-1}$ (with $\|\cdot\|$ induced by g) we have

$$\exp_d(v) = \cos(\|v\|)d + \sin(\|v\|)\frac{v}{\|v\|} \quad \forall v \in T_d S^{n-1} \setminus \{0\}.$$

The exponential map is always smooth, and by the inverse function theorem it possesses a smooth local inverse defined on some open neighborhood M_x of $x \in M$. This inverse is called the *logarithm map*, $\log_x: M_x \rightarrow T_x M$. Moreover, further logarithm maps may exist as local inverses of \exp_x on neighborhoods of other image points $\exp_x(v) \notin M_x$.

For PGA it is crucial that \exp_x is globally defined and surjective, and that local inverses exist almost everywhere on M : given a smooth curve $c: [0, 1] \rightarrow M$ starting at $c(0) = x$, we seek a smooth curve $y: [0, 1] \rightarrow T_x M$ such that $\exp_x(y(t)) = c(t)$ for all $t \in [0, 1]$. To construct that *lifted* curve y , we need one or more logarithm maps such that the closures of their domains of definition cover the image of c . Concrete representations of logarithm maps and lift maps for the manifolds of interest will be given in Sections 3.2 and 3.3.

All the concepts above remain valid when intersecting M with an open subset \mathcal{U} of \mathbb{R}^n . This still gives quite special submanifolds of \mathbb{R}^n , and we will use it below. More generally, all concepts extend to manifolds that are patched together from overlapping pieces of the form $M \cap \mathcal{U}$, even without a surrounding linear space, and even in infinite dimension.

3.2. Directors and Rotations. Our first manifold of interest is the set of directors in \mathbb{R}^3 , the unit 2-sphere $S^2 = \{d \in \mathbb{R}^3: \|d\|_2 = 1\}$, which has already served as an illustrative example. Recall the properties

$$\begin{aligned} T_d S^2 &= \{d\} \times \{v \in \mathbb{R}^3: \langle d, v \rangle = 0\} \cong \{d\}^\perp, \\ \exp_d(v) &= \begin{cases} d, & \|v\| = 0, \\ \cos(\|v\|)d + \sin(\|v\|)\frac{v}{\|v\|}, & \|v\| > 0. \end{cases} \end{aligned} \quad (3)$$

Clearly we have $\exp_d(v) = -d$ for every tangent vector of length $\|v\| = \pi$, and the open disk $D_\pi := \{v \in T_d S^2: \|v\| < \pi\}$ is actually a maximal domain of injectivity of \exp_d . Now the logarithm map $\log_d: S^2 \setminus \{-d\} \rightarrow D_\pi$ has the explicit representation

$$\log_d(e) = (d, v), \quad v := \begin{cases} 0, & \|e - \langle d, e \rangle d\|_2 = 0, \\ \arccos\langle d, e \rangle \frac{e - \langle d, e \rangle d}{\|e - \langle d, e \rangle d\|_2}, & \|e - \langle d, e \rangle d\|_2 > 0, \end{cases} \quad (4)$$

where $e - \langle d, e \rangle d$ is the projection of e on $\{d\}^\perp$ and $\|v\| = \arccos\langle d, e \rangle \in (0, \pi)$ is the angle between d and e . Further logarithm maps and the construction of a lift map will be discussed in Section 3.3.

Our second manifold of interest is the matrix group of *rotations* in \mathbb{R}^3 , called the *special orthogonal group* $SO(3)$. This is a (non-commutative) multiplicative group and also a 3-dimensional manifold in the matrix space $\mathbb{R}^{3 \times 3}$ seen as the vector space \mathbb{R}^9 . To understand

the basic structure, we first define the *orthogonal group*

$$O(3) := \{R \in \mathbb{R}^{3 \times 3}: R^T R = I\}.$$

When viewing the matrix R as a triple of mutually orthogonal directors, $R = [d_1 \ d_2 \ d_3]$, the symmetric matrix constraint $R^T R = I$ is equivalently written as

$$\|d_1\|_2^2 = \|d_2\|_2^2 = \|d_3\|_2^2 = 1, \quad \langle d_1, d_2 \rangle = \langle d_1, d_3 \rangle = \langle d_2, d_3 \rangle = 0.$$

Thus $O(3)$ is a 3-dimensional submanifold in the 9-dimensional matrix space $\mathbb{R}^{3 \times 3} \cong \mathbb{R}^9$. The determinant of an orthogonal matrix is either $+1$ or -1 , and hence $O(3)$ consists of two disconnected parts. Now let $\mathcal{U}_+ := \{R \in \mathbb{R}^{3 \times 3}: \det(R) > 0\}$ (which is open) and define

$$SO(3) := O(3) \cap \mathcal{U}_+ = \{R \in \mathbb{R}^{3 \times 3}: R^T R = I, \det(R) = 1\}.$$

This is still a manifold with a group structure, called a *Lie group*. On Lie groups it suffices to consider as a “universal” tangent space the one at the neutral element, the *Lie algebra*, since every tangent space has a natural representation in terms of it. In our case, that representation at the identity matrix I reads

$$T_R SO(3) = \{RN: N \in A(3)\} = RT_I SO(3) = R\mathfrak{so}(3),$$

where $A(3)$ denotes the space of *antisymmetric* (or *skew-symmetric*) matrices, $A(3) := \{N \in \mathbb{R}^{3 \times 3}: N^T = -N\}$, and $\mathfrak{so}(3)$ is the standard notation for the Lie algebra of $SO(3)$. We also use the more succinct notation RN for $(R, RN) \in T_R SO(3)$. As Riemannian metric on $\mathbb{R}^{3 \times 3}$ and hence on $SO(3)$ we choose a scaled Frobenius scalar product (so that $\|N\|$ becomes the rotation angle of $\exp(N)$, see below),

$$\langle V, W \rangle := \frac{\langle V, W \rangle_F}{2} = \frac{\text{Tr}(V^T W)}{2}, \quad g(R)(RN_1, RN_2) = \langle RN_1, RN_2 \rangle = \langle N_1, N_2 \rangle.$$

Thus, $T_R SO(3)$ is a subspace of the 8-dimensional orthogonal complement of $\text{span}\{R\}$,

$$\{R\}^\perp = \{RV \in \mathbb{R}^{3 \times 3}: 0 = \langle R, RV \rangle = \frac{1}{2} \text{Tr}(V)\}.$$

Now the exponential map $\exp: \mathfrak{so}(3) \rightarrow SO(3)$ is the standard matrix exponential, and due to the identity $N^3 = -\|N\|^2 N$ (with $\|\cdot\|$ induced by g) it has the explicit representation

$$\exp(N) = \sum_{k=0}^{\infty} \frac{1}{k!} N^k = \begin{cases} I, & \|N\| = 0, \\ I + \frac{\sin\|N\|}{\|N\|} N + \frac{1 - \cos\|N\|}{\|N\|^2} N^2, & \|N\| > 0. \end{cases} \quad (5)$$

It is globally defined and surjective. With $\theta := \|N\|$ and $U := N/\theta$ for $\theta > 0$, the last formula explains the so-called *axis-angle representation* $N = \theta U$ of the rotation $\exp(N)$,

$$\exp(N) = \exp(\theta U) = I + (\sin \theta)U + (1 - \cos \theta)U^2. \quad (6)$$

To understand this fundamental geometric interpretation, consider a rotation axis given by a director $u \in S^2$ and a rotation angle $\theta \in \mathbb{R}$. Then the rotation about axis u with angle θ is given by the *rotation vector* (or *Euler vector*) $n = \theta u$ as $\exp(N)$ where

$$N = \theta U = \theta \text{skew}(u) = \text{skew}(n) := \begin{bmatrix} 0 & -n_3 & n_2 \\ n_3 & 0 & -n_1 \\ -n_2 & n_1 & 0 \end{bmatrix}.$$

Note that our definition of g makes the isomorphism $\text{skew}: \mathbb{R}^3 \cong A(3) \cong \mathfrak{so}(3)$ *isometric*, i.e., $\|N\| = \|n\|_2 = \theta$. We identify U with the unit axis u by virtue of this isometry and note that $Uv = u \times v$ for each $v \in \mathbb{R}^3$, where $u \times v$ denotes the cross product.

Using the notation $R(U, \theta) = \exp(\theta U)$, the identity (6) readily implies several geometrically obvious symmetries of $SO(3)$ from which much of the subsequent theory derives:

$$\begin{aligned} R(-U, -\theta) &= R(U, \theta), \\ R(U, \theta + 2k\pi) &= R(U, \theta) \quad \forall k \in \mathbb{Z}, \end{aligned}$$

and the direct implications

$$\begin{aligned} R(-\mathbf{U}, \pi) &= R(\mathbf{U}, -\pi) = R(\mathbf{U}, \pi), \\ R(-\mathbf{U}, \pi - \theta) &= R(\mathbf{U}, \theta - \pi) = R(\mathbf{U}, \pi + \theta). \end{aligned}$$

The geodesics $c: \mathbb{R} \rightarrow SO(3)$ are precisely the curves $c(t) := R \exp(t\mathbf{N})$ with arbitrary $\mathbf{N} \in \mathfrak{so}(3)$ and $c(0) = R$. The velocity is $\dot{c}(t) = c(t)\mathbf{N}$ so that $\dot{c}(0) = R\mathbf{N}$. All geodesics are closed curves with period $2\pi/\|\mathbf{N}\|$, except for the constant ones (with $\mathbf{N} = 0$).

A maximal domain of injectivity of \exp is the open ball $B_\pi := \{\mathbf{N} \in \mathfrak{so}(3) : \|\mathbf{N}\| < \pi\}$ whereas every pair of antipodal points $\pm\pi\mathbf{U} \in \partial B_\pi$ maps to the same rotation $\exp(\pi\mathbf{U})$. Hence we have a unique local inverse, the logarithm map $\log: SO(3) \setminus \exp(\partial B_\pi) \rightarrow B_\pi$, which is given by the explicit representation

$$\log(R) = \begin{cases} 0, & R = I, \\ \frac{\theta}{\sin \theta} \frac{R - R^T}{2}, & \theta := \arccos \frac{\text{Tr}(R) - 1}{2}, \quad R \neq I. \end{cases} \quad (7)$$

Here $\theta \in [0, \pi)$ is again the rotation angle. We finally note that $\exp_R(R\mathbf{N}) = R \exp(\mathbf{N})$ and $\log_R(RS) = R \log(S)$ for all $R, S \in SO(3)$ and $\mathbf{N} \in \mathfrak{so}(3)$. Further logarithm maps and the construction of a lift map will again be discussed in Section 3.3.

3.3. Singularities and Lifts. Here we take a deeper look at the exponential maps and associated logarithm maps on S^2 and $SO(3)$. The issues to be discussed are caused by the *rotational symmetries* and by the *compactness* that both manifolds exhibit: the respective exponential maps “wrap their tangent space around the manifold” infinitely often. Therefore the inverses of the exponential maps are not unique (in fact they have infinitely many possible values at certain singularities) and hence we may need several logarithm maps to lift a curve by “unwrapping” the tangent space.

Turning first to the 2-sphere S^2 , we fix an element d and denote by D_r the open circular disk of radius r in $T_d S^2$. Next we define annuli $A_0 := D_\pi \setminus \{0\}$ and $A_k := D_{(k+1)\pi} \setminus \bar{D}_{k\pi}$ for $k > 0$, where \bar{D}_r denotes the closure of D_r . Then every tangent vector $v \in A_k$ has a unique axis-angle representation $v = \theta\mathbf{u}$ with $\|\mathbf{u}\| = 1$ and $\theta = \|v\| \in (k\pi, (k+1)\pi)$, and hence we can define smooth bijections $\Phi_{k\ell}: A_k \rightarrow A_\ell$ such that $\exp_d(\Phi_{k\ell}(v)) = \exp_d(v)$:

$$\Phi_{k\ell}(v) = \Phi_{k\ell}(\theta\mathbf{u}) := \begin{cases} [(\ell - k)\pi + \theta]\mathbf{u}, & \ell - k \text{ even}, \\ [(\ell + k + 1)\pi - \theta](-\mathbf{u}), & \ell - k \text{ odd}. \end{cases}$$

In Section 3.2 we have already seen that \exp_d maps D_π bijectively to $S^2 \setminus \{-d\}$ and the entire boundary ∂D_π to $-d$. More generally, \exp_d maps every annulus A_k bijectively to $S^2 \setminus \{-d, +d\}$, every “even” boundary $\partial D_{2k\pi}$ to $+d$, and every “odd” boundary $\partial D_{(2k+1)\pi}$ to $-d$. This yields infinitely many distinct *branches* of the logarithm map (see Fig. 1),

$$\log_{d,k}: S^2 \setminus \{\pm d\} \rightarrow A_k, \quad \log_{d,k}(e) := \Phi_{0k}(\log_d(e)),$$

where $\log_{d,0}$ agrees with the *principal branch* \log_d except that $\log_{d,0}(d)$ is not defined. Clearly, the closures \bar{A}_k cover the tangent space, $T_d S^2 = \bigcup_{k \in \mathbb{N}} \bar{A}_k$, and hence it should be possible to lift smooth curves from S^2 to $T_d S^2$ by switching from $\log_{d,k}$ to $\log_{d,k \pm 1}$ whenever the lifted curve $y(t)$ crosses ∂A_k . However, $\log_{d,k}$ has singularities at $\pm d$ where the projection $e - \langle d, e \rangle d$ in (4) vanishes and the image point in ∂A_k is not unique. These singularities can prevent the construction of a smooth lift. In fact, a curve that enters $-d$ at zero speed along a geodesic circle and exits along another one will have a discontinuous lift, and a curve that stays at $-d$ for a positive time will have an undefined lift. The same happens at $+d$ unless the lifted point in $T_d S^2$ is the origin. As a sufficient condition for a unique smooth lift we require that $y(t)$ crosses ∂A_k at nonzero speed, i.e., $\dot{c}(t) \neq 0$ whenever $c(t) = \pm d$. In that case, $\dot{y}(t)$ is necessarily orthogonal to ∂A_k .

On $SO(3)$ we face an essentially similar though slightly more complicated situation. By B_r we denote the open ball of radius r in $\mathfrak{so}(3)$. Then we define the open spherical

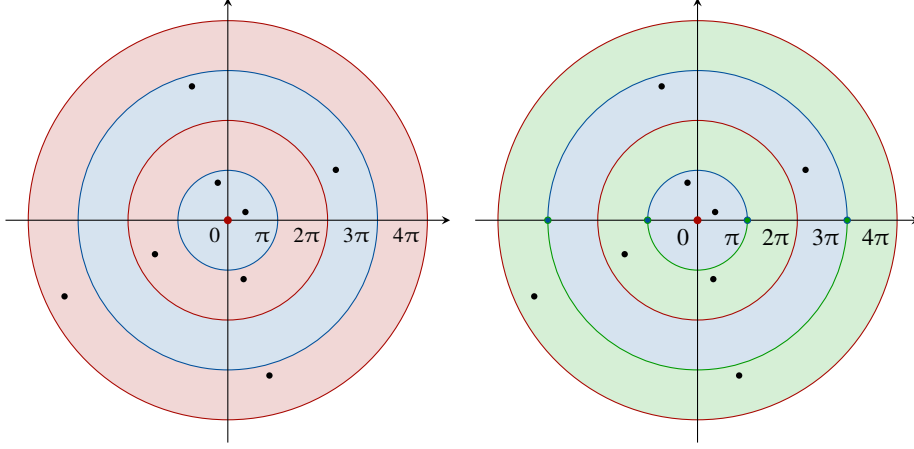


FIGURE 1. Tangent space $T_d S^2$ (left) and a 2d subspace of $\mathfrak{so}(3)$ (right). Light colored rings show maximal injectivity sets of \exp_d resp. \exp . Red circles show “even” boundaries that are mapped to d resp. I ; blue circles (left) and antipodal blue-green half circles (right) show “odd” boundaries that are mapped to $-d$ (left) or $\exp(\partial B_\pi)$ (right). Two sets of black dots on radial lines show \log_0, \dots, \log_3 of two elements of S^2 resp. $SO(3)$.

shells $S_0 := B_\pi \setminus \{0\}$ and $S_k := B_{(k+1)\pi} \setminus \bar{B}_{k\pi}$ for $k > 0$. Using the unique angle-axis representation $N = \theta U$ of a matrix $N \in S_k$, where $\theta \in (k\pi, (k+1)\pi)$, we have again smooth bijections $\Phi_{k\ell}: S_k \rightarrow S_\ell$ such that $\exp(\Phi_{k\ell}(\theta U)) = \exp(\theta U)$:

$$\Phi_{k\ell}(N) = \Phi_{k\ell}(\theta U) := \begin{cases} [(\ell - k)\pi + \theta]U, & \ell - k \text{ even,} \\ [(\ell + k + 1)\pi - \theta](-U), & \ell - k \text{ odd.} \end{cases}$$

Now \exp maps $\partial B_{k\pi}$ entirely to I for even k and maps antipodal points on $\partial B_{k\pi}$ to the same image point for odd k . Finally S_k is bijectively mapped to $SO(3) \setminus \exp(\partial S_k)$, and we obtain again a sequence of distinct branches of the logarithm map,

$$\log_k: SO(3) \setminus \exp(\partial S_k) \rightarrow S_k, \quad \log_k(R) := \Phi_{0k}(\log(R)).$$

Again \log_0 is undefined at $R = I$ but otherwise identical to the *principal branch* \log . For an illustration in $\mathbb{R}^3 \cong \mathfrak{so}(3)$ see Fig. 1. Note that each image set $\exp(\partial S_k)$ contains the identity I as image of the entire “even” boundary. In contrast, the image of each “odd” boundary is the 2-dimensional submanifold $\Pi := \exp(\partial B_\pi)$ in $SO(3)$: the geodesic sphere of all rotations at distance π to I . Moreover, it is immediate from (6) that Π is also a sphere at Euclidian distance 2 from I in $\mathbb{R}^{3 \times 3}$:

$$\|\exp(\pi U) - I\|^2 = \|2U^2\|^2 = 2 \operatorname{Tr}(U^T U^T U U) = 2 \operatorname{Tr}(U^T U) = 4\|U\|^2 = 4.$$

Thus, both S^2 and $SO(3)$ have geodesic diameter π and Euclidian diameter 2 (as respective subsets of \mathbb{R}^3 and $\mathbb{R}^{3 \times 3}$), but every point d in S^2 has the single antipodal point $-d$ whereas every matrix R in $SO(3)$ has a 2-sphere of most distant matrices: the set $R\Pi$ (which can be shown to be centered at $-\frac{1}{3}R$ with radius $2/\sqrt{3}$). In fact, the antipodal matrix $-R$ is always an element of $O(3)$ outside $SO(3)$, at Euclidian distance $\sqrt{6}$.

Finally, as before, the closures of the domains of the logarithm maps cover the entire tangent space, $\mathfrak{so}(3) = \bigcup_{k \in \mathbb{N}} \bar{S}_k$, but we have singularities at the boundaries where the denominator $\sin \theta$ in (7) vanishes and the image in ∂S_k is not unique. To obtain unique and smooth lifts, we again require $\dot{c}(t) \neq 0$ whenever $c(t) \in \exp(\partial S_k) = \{I\} \cup \Pi$.

Note that, due to the rotational symmetry of S^2 , we might also lift a curve $c: I \rightarrow S^2$ into $\mathfrak{so}(3)$ by setting $c(t) =: R(t)c(0)$. This defines a unique curve $R: I \rightarrow SO(3)$ that gives

the desired lift $N: I \rightarrow \mathfrak{so}(3)$. Then c is recovered as $c(t) = \exp(N(t))c(0)$. We do not explore this relation further; the underlying mathematical property is that the symmetric space S^2 becomes a homogeneous space under the group action of $SO(3)$.

We conclude this section by noting that the following orthogonal projections are defined for S^2 and $SO(3)$ as respective submanifolds of \mathbb{R}^3 and $\mathbb{R}^{3 \times 3}$: given $x \in \mathbb{R}^3 \setminus \{0\}$, the orthogonal projection is

$$\frac{x}{\|x\|_2} \in S^2. \quad (8)$$

Given $B \in \mathbb{R}^{3 \times 3}$ with $\det(B) > 0$ and with singular value decomposition $B = U\Sigma V^T$, the orthogonal projection is

$$UV^T \in SO(3). \quad (9)$$

4. NUMERICAL IMPLEMENTATION OF PGA

In this section we discuss the numerical implementations of the exponential map and of the principal branch of the logarithm map for our manifolds of interest:

$$\begin{aligned} \exp_d: T_d S^2 &\rightarrow S^2, & \exp: \mathfrak{so}(3) &\rightarrow SO(3), \\ \log_d: S^2 \setminus \{-d\} &\rightarrow D\pi \subset T_d S^2, & \log: SO(3) \setminus \Pi &\rightarrow B\pi \subset \mathfrak{so}(3). \end{aligned}$$

For the logarithms we have to take special care in the vicinity of their singularities. Later on we construct the corresponding lifts of discrete snapshots $x_i = c(t_i)$ of a smooth curve $c: [t_0, t_n] \rightarrow M$ for $M = S^2$ and $M = SO(3)$. We assume that c itself is not given and define the discrete lift y_0, \dots, y_n as follows. Set $y_0 := 0$ in $T_{x_0}M$. For $i = 1, \dots, n$, lift the geodesic segment from x_{i-1} to x_i into $T_{x_0}M$ so that the lift starts at y_{i-1} , and define its endpoint as y_i . We call this step the *lift map*, denoted as $\text{lift}_{x_0, y_{i-1}}(x_i)$. On S^2 and $SO(3)$, the geodesic segment from x_{i-1} to x_i is unique and hence the lift map is well-defined if the geodesic distance of x_{i-1} and x_i is less than π : we have $c_{d_0 d_1}(t) = \exp_{d_0}(t \log_{d_0}(d_1))$ on S^2 and $c_{R_0 R_1}(t) = \exp_{R_0}(t \log_{R_0}(R_1)) = R_0 \exp(t \log(R_0^T R_1))$ on $SO(3)$. The difficulty is that we have to decide numerically whether the geodesic segment crosses a singularity (the lifted curve crosses ∂A_k in $T_d S^2$ or ∂S_k in $\mathfrak{so}(3)$) in order to determine the proper branch of \log for y_i .

All numerical issues discussed below refer to double precision floating point arithmetic (64 bit numbers in IEEE 754 format).

4.1. Directors and Rotations. Starting with S^2 , we implement the exponential map \exp_d essentially according to (3),

$$\theta := \|v\|_2, \quad \exp_d(v) = \begin{cases} d, & \theta \leq \varepsilon_M, \\ (\cos \theta)d + \frac{\sin \theta}{\theta}v, & \theta > \varepsilon_M. \end{cases} \quad (10)$$

Note that we use the machine precision $\varepsilon_M > 0$ as threshold in the case distinction to guard against roundoff errors. For $\varepsilon_M = 0$ (exact arithmetic) this gives precisely definition (3). The logarithm map is implemented according to (4) with a second threshold $\delta \in (0, 1)$,

$$\begin{aligned} c &:= \langle d, e \rangle, \\ p &:= e - cd, \\ s &:= \|p\|_2, \end{aligned} \quad \log_d(e) = \begin{cases} 0, & s \leq \varepsilon_M, \\ (\frac{1}{s} \arccos c)p, & s > \varepsilon_M, c > -1 + \delta, \\ (\arccos c)(\frac{1}{s}p), & s > \varepsilon_M, c \leq -1 + \delta. \end{cases} \quad (11)$$

Note that we have $c = \cos \theta$ and $s = \sin \theta$ where $\theta \in (0, \pi]$ is the angle between d and e , which implies $1/s \rightarrow \infty$ for $\theta \rightarrow 0$ and for $\theta \rightarrow \pi$. The evaluation order in case 3 would suffice to avoid the singularity in both cases since $\frac{1}{s}p \in S^2$. However, for $\theta \gtrsim 0$ we prefer case 2 as it saves two divisions while remaining stable: $\frac{1}{s} \arccos c = \theta / \sin \theta \approx 1$. Hence the value of δ is irrelevant in exact arithmetic, and for $\varepsilon_M = 0$ we obtain the original

definition (4). Implementing the lift from S^2 into $T_d S^2$ is less straightforward and will be discussed in Section 4.2.

How do we determine the threshold value δ ? Our goal is to use case 3 only when necessary while keeping the *lift-and-project* error $\|\exp_d(\log_d(e)) - e\|_\infty$ as small as possible for all $d, e \in S^2$. To this end, we perform numerical experiments with 9 260 592 directors in 3 086 864 rotation matrices from the four $SO(3)$ examples in Section 5. We pick the smallest negative power of 2 such that case 3 is consistently more accurate than case 2 for $c \in [-1, -1 + \delta]$. This yields the value

$$\delta = 2^{-21} = 2^{31} \varepsilon_M = 32\sqrt{\varepsilon_M}.$$

In $SO(3)$ we implement the exponential map according to (5) and (6),

$$\begin{aligned} \theta &:= \|\mathbf{N}\|, & \exp(\mathbf{N}) &= \begin{cases} \mathbf{I}, & \theta \leq \varepsilon_M, \\ \mathbf{I} + (\sin \theta)\mathbf{U} + (1 - \cos \theta)\mathbf{U}^2, & \theta > \varepsilon_M. \end{cases} \end{aligned} \quad (12)$$

As in (10), $\varepsilon_M > 0$ guards against roundoff errors and $\varepsilon_M = 0$ recovers the exact definition. Of course, the axis matrix \mathbf{U} is only computed in case 2.

The logarithm map (7) requires again a more careful case distinction for $\theta \gtrsim 0$ and for $\theta \lesssim \pi$. In the case $\theta \gtrsim 0$ we set $\log(\mathbf{R}) = 0$ if θ is extremely small, otherwise we use the approximation $\mathbf{R} = \exp(\mathbf{N}) \approx \mathbf{I} + \mathbf{N}$, giving $\mathbf{N} = \frac{1}{2}(\mathbf{N} - \mathbf{N}^\top) \approx \frac{1}{2}(\mathbf{R} - \mathbf{R}^\top)$. In the case $\theta \lesssim \pi$ we also need to choose the sign of \mathbf{U} , i.e., one of the two possible directions of the axis. We use the approximation $\mathbf{R} \approx \exp(\pi\mathbf{U}) = \mathbf{I} + 2\mathbf{U}^2 = 2\mathbf{u}\mathbf{u}^\top - \mathbf{I}$ to determine $|\mathbf{u}|$ from the *diagonal* entries of \mathbf{R} and the signs of \mathbf{u}_i from the *off-diagonal* entries, as follows. Set $\mathbf{u}_i := (\frac{1}{2}R_{ii} + \frac{1}{2})^{1/2}$. If $R_{21} < 0$, flip \mathbf{u}_2 to $-\mathbf{u}_2$. If $R_{31} < 0$ or $R_{32} < 0 \wedge \mathbf{u}_1 = 0$, flip \mathbf{u}_3 to $-\mathbf{u}_3$. Call the result $\mathbf{u}(\mathbf{R})$. Its first nonzero entry will be positive, that is, the axis direction is fixed by requiring $\mathbf{u}(\mathbf{R})$ to be *lexicographically positive*. Now implement \log as follows with thresholds $\delta_1, \delta_2, \delta_3 \in (0, 1)$,

$$\begin{aligned} c &:= \frac{\text{Tr}(\mathbf{R}) - 1}{2}, & \log(\mathbf{R}) &= \begin{cases} 0, & c \in [1 - \delta_1, 1], \\ \frac{1}{2}(\mathbf{R} - \mathbf{R}^\top), & c \in [1 - \delta_2, 1 - \delta_1], \\ \frac{1}{2}(\theta/\sin \theta)(\mathbf{R} - \mathbf{R}^\top), & c \in (-1 + \delta_3, 1 - \delta_2), \\ \pi \text{skew}(\mathbf{u}(\mathbf{R})), & c \in [-1, -1 + \delta_3]. \end{cases} \end{aligned} \quad (13)$$

Here θ is only computed in case 3, and setting $\delta_1 = \delta_2 = \delta_3 = 0$ recovers definition (7). Again the threshold values are chosen as the smallest negative powers of 2 that minimize the lift-and-project error $\|\exp(\log(\mathbf{R})) - \mathbf{R}\|_{\max}$, where $\|\cdot\|_{\max}$ on $\mathbb{R}^{3 \times 3}$ is $\|\cdot\|_\infty$ on \mathbb{R}^9 . We obtain the values

$$\delta_1 = 2^{-50} = 4\varepsilon_M, \quad \delta_2 = 2^{-42} = 1024\varepsilon_M, \quad \delta_3 = 2^{-28} = 2^{24}\varepsilon_M = \frac{1}{4}\sqrt{\varepsilon_M}.$$

In the numerical experiments we use the same 3 086 864 rotation matrices as above; see Section 5. Considering the value $c = \frac{1}{2}(\text{Tr}(\mathbf{R}) - 1)$ of these matrices, 59 are in the range $[1 - 16\varepsilon_M, 1)$ relevant for δ_1 , 278 are in the range $(1 - 4096\varepsilon_M, 1 - 16\varepsilon_M)$ relevant for δ_2 , and 68 are in the range $(-1, -1 + \sqrt{\varepsilon_M}]$ relevant for δ_3 .

4.2. Lifts and Singularities. To construct $\text{lift}_{d, \theta\mathbf{u}}(e)$ for $d, e \in S^2$ and $\theta\mathbf{u} \in \bar{A}_k \subset T_d S^2$ numerically, we first check whether $e = \pm d$ holds numerically to return a vector on the appropriate part of ∂A_k ; see Algorithm 1. Otherwise we compute the quantities c, p, s and the angle $\arccos c$ of $\log_d(e)$ from (11) to determine the proper branch ℓ for $\text{lift}_{d, \theta\mathbf{u}}(e) = \log_{d, \ell}(e) = \Phi_{0\ell}(\log_d(e))$ and return the result. Here the axis-angle decomposition $\theta\mathbf{u}$ is unique except in the case $\theta = 0$ where \mathbf{u} is arbitrary and we simply choose $\mathbf{u} = 0$.

The lift of a sequence of elements $x_0, \dots, x_n \in M$ into $T_{x_0}M$ is given in Algorithm 2. In the algorithms we use the parameters $\tau_1 = 8\varepsilon_M$ (the current snapshot is numerically identical to the last one), $\tau_2 = \varepsilon_M$ (geodesic passes through $\pm d$), and $\tau_3 = 4\varepsilon_M$ (geodesic

Algorithm 1: Lift map for S^2 : $\text{lift}_{d,\theta u}(e)$.

Input : directors $d, e \in S^2$, tangent vector $\theta u \in \bar{A}_k \subset T_d S^2$ in axis-angle form
Output: lift $v \in T_d S^2$ of e with respect to θu

```

1  $c := \langle d, e \rangle$ ;
2  $\text{odd} := k \bmod 2$  (0 or 1);
3 if  $1 - c \leq \tau_3$  then ( $e \approx +d$ : choose  $v$  on “even” component of  $\partial A_k$ )
4    $\text{return } v := (k + \text{odd})\pi u$ ;
5 if  $1 + c \leq \tau_3$  then ( $e \approx -d$ : choose  $v$  on “odd” component of  $\partial A_k$ )
6    $\text{return } v := (k + 1 - \text{odd})\pi u$ ;
7  $\ell := k$ ;
8  $\phi := \arccos c$ ;
9  $p := e - cd$ ,  $w := (-1)^k p / \|p\|_2$ ;
10 if  $\langle u, w \rangle + 1 \leq \tau_2$  then (geodesic passes through  $\pm d$ )
11    $w := -w$ ;
12   if  $\|((\ell + 2 - \text{odd})\pi - (-1)^k \phi)w - \theta u\|_2 < \pi$  and ( $k > 0$  or  $\phi > 1$ ) then
13      $\ell := \ell + 1$ ;
14   else
15     if  $\ell == 0$  then (prevent change to negative branch)
16        $w := -w$ ;
17     else
18        $\ell := \ell - 1$ ;
19    $\text{odd} := \ell \bmod 2$ ;
20  $\phi := (\ell + \text{odd})\pi + (-1)^k \phi$ ;
21 return } v := \phi w;

```

Algorithm 2: Lift of discrete snapshots from a manifold M .

Input : samples $x_0, \dots, x_n \in M$
Output: lift $v_0, \dots, v_n \in T_{x_0} M$

```

1  $v_0 := 0$ ;
2 for  $i = 1, \dots, n$  do
3   if  $\text{dist}(x_i, x_{i-1}) \leq \tau_1$  then ( $x_i, x_{i-1}$  are numerically identical)
4      $v_i := v_{i-1}$ ;
5   else
6      $v_i := \text{lift}_{x_0, v_{i-1}}(x_i)$ ;

```

is close to one of the two singularities at $\pm d$). All parameters have been determined by numerical experiments.

To construct the lift map for $SO(3)$ numerically, we compute the numerical logarithm map (13) in the following axis-angle form with $c = \frac{1}{2}(\text{Tr}(R) - 1)$, $V := R - R^T$:

$\theta = 0,$	$U = 0,$	case 1,
$\theta = \ V\ /2,$	$U = V/\theta,$	case 2,
$\theta = \arccos c,$	$U = V/(2\sqrt{1 - c^2}),$	case 3,
$\theta = \pi,$	$U = \text{skew}(u(R)),$	case 4.

Algorithm 3: Lift map for $SO(3)$: $\text{lift}_N(\mathbf{R})$.

Input : tangent matrix $\mathbf{N} \in \mathfrak{so}(3)$, rotation matrix $\mathbf{R} \in SO(3)$
Output: lift $\theta\mathbf{U}$ of \mathbf{R} with respect to \mathbf{N}

```

1  $\theta_0 := \|\mathbf{N}\|$ ;
2  $\theta\mathbf{U} := \log(\mathbf{R})$  (initial axis-angle-form: a bijection  $\Phi_{0\ell}$  may be applied later);
3 if  $\theta_0 + \theta < \pi$  then
4   return  $\theta\mathbf{U}$ 
5  $s := \langle \mathbf{N}, \mathbf{U} \rangle$ ;
6 if  $\|s - \theta_0\| < 8\epsilon_{O(3)}\theta_0$  then ( $\mathbf{N}, \mathbf{U}$  are numerically linearly dependent)
7   if  $s < 0$  then  $\bar{\theta} := -\theta$ ;
8   else  $\bar{\theta} := +\theta$ ;
9   if  $\theta_0 - \bar{\theta} < \pi$  then
10    return  $\theta\mathbf{U}$ 
11    $\ell := \lfloor (\theta_0 - \bar{\theta})/\pi \rfloor$ ;
12   if  $\ell$  is odd then  $++\ell$ ;
13   if  $\bar{\theta} > 0$  then
14     return  $+(\bar{\theta} + \ell\pi)\mathbf{U}$ 
15   else
16     return  $-(\bar{\theta} + \ell\pi)\mathbf{U}$ 
17  $k := \ell := \lfloor \theta_0/\pi \rfloor$ ;
18  $\text{odd} := k \bmod 2$ ;
19 if  $k \neq 0$  then
20    $\mathbf{N} := [1 - (k + \text{odd})\pi/\theta_0]\mathbf{N}$ 
21 if  $\|\theta\mathbf{U} - \mathbf{N}\| > \|(\theta - 2\pi)\mathbf{U} - \mathbf{N}\|$  then
22   if  $\text{odd}$  then  $--\ell$ ;
23   else  $++\ell$ ;
24 if  $\ell$  is odd then  $\theta := \theta - (\ell + 1)\pi$ ;
25 else  $\theta := \theta + \ell\pi$ ;
26 return  $\theta\mathbf{U}$ 

```

Again \mathbf{U} is arbitrary in the case $\theta = 0$ and we have chosen $\mathbf{U} = 0$. Then, given $\mathbf{N} \in \mathfrak{so}(3)$, we need to determine the proper branch ℓ for $\text{lift}_N(\mathbf{R}) = \log_\ell(\mathbf{R}) = \Phi_{0\ell}(\theta\mathbf{U})$ where we distinguish three cases, see Algorithm 3: *i*) if $\|\mathbf{N}\| + \theta < \pi$, then $\ell = 0$ (quick return); *ii*) if \mathbf{N} and \mathbf{U} are linearly dependent, then $\exp(\mathbf{N})$ and \mathbf{R} are rotations about a common axis and the computation of ℓ simplifies; and *iii*) otherwise we have the slightly more complicated general case. Note that “even” branch boundaries at angles $2k\pi$ (red in Fig. 1) can only be crossed in case *ii*). In Algorithm 3 we use the parameter $\epsilon_{O(3)} = 8\epsilon_M$, which is the best accuracy that can be guaranteed for the numerical representation of orthogonal matrices with respect to the *orthogonality error* $e_\perp(\mathbf{R}) := \|\mathbf{R}^T\mathbf{R} - \mathbf{I}\|_{\max}$, as determined by numerical experiments; cf. Section 4.4.

4.3. PCA in the Tangent Space. In dynamics of hybrid mechanical systems we typically perform PGA on a *product manifold* of the form $\mathcal{M} = (\mathbb{R}^3 \times SO(3))^{K_1} \times (\mathbb{R}^3 \times S^2)^{K_2} \times (\mathbb{R}^3)^{K_3}$ that results from a combination of rigid bodies and finite element discretizations of beams, shells, and 3-dimensional elastic bodies, or possibly on a submanifold of \mathcal{M} arising due to holonomic constraints. The principal component analysis in the tangent space $T_{x_0}\mathcal{M}$ is performed on the *snapshot matrix* obtained from lifting $x_1, \dots, x_n \in \mathcal{M}$

where $x_i = c(t_i)$:

$$Y := [y_1 \ \dots \ y_n] \in (T_{x_0}M)^n \cong \mathbb{R}^{m \times n}. \quad (14)$$

Then, as usual, we compute the singular value decomposition (SVD)

$$Y = U\Sigma V^T = \sum_{j=1}^r \sigma_j u_j v_j^T, \quad r = \text{rank } Y \leq \min(m, n),$$

where $U \in O(m)$ and $V \in O(n)$ are orthogonal matrices that contain the left and right *singular vectors* u_j and v_j , respectively, and $\Sigma \in \mathbb{R}^{m \times n}$ is a rectangular diagonal matrix that contains the *singular values* $\sigma_1 \geq \dots \geq \sigma_r > 0$. Best rank p approximations of Y with respect to both the spectral norm $\|\cdot\|_2$ and the Frobenius norm $\|\cdot\|_F$ are then obtained for each $p \leq r$ by the *truncated SVD*

$$Y_p = U\Sigma_p V^T = \sum_{j=1}^p \sigma_j u_j v_j^T. \quad (15)$$

The matrices $\sigma_j u_j v_j^T$ in this sum are the p principal components (or principal modes) of the lifted discrete trajectory represented by Y . The resulting approximated snapshots in M are finally obtained by mapping the columns y_{pk} of the matrix Y_p back to M ,

$$x_{pk} = c_p(t_k) = \exp_{x_0}(y_{pk}), \quad y_{pk} = Y_p e_k = \sum_{j=1}^p \sigma_j u_j v_{jk}, \quad k = 1, \dots, n. \quad (16)$$

Note that the reference point x_0 does not change here: it is the given initial point of the discrete trajectory, and it always maps to $y_0 = 0 \in T_{x_0}M$ which we have therefore dropped in forming Y .

The situation is different when considering multiple trajectories of a dynamic system simultaneously. In that case we compute a (not necessarily unique) *intrinsic mean* \bar{x} of all points on all k discrete trajectories [6],

$$\sum_{i=1}^k \sum_{j=0}^{n_i} d_M(x_{ij}, \bar{x})^2 \stackrel{!}{=} \min_{x \in M} \sum_{i=1}^k \sum_{j=0}^{n_i} d_M(x_{ij}, x)^2,$$

we do not drop any initial points, and the snapshot matrix contains the entire set of concatenated trajectories lifted into the tangent space at the mean \bar{x} :

$$Y := [y_{10} \ \dots \ y_{1n_1} \ \dots \ y_{k0} \ \dots \ y_{kn_k}] \in (T_{\bar{x}}M)^n \cong \mathbb{R}^{m \times n},$$

$$n := (n_1 + 1) + \dots + (n_k + 1).$$

The intrinsic mean is typically computed by a gradient descent algorithm with fixed step length α where the iterate \bar{x}_ℓ is updated by the rule

$$\bar{x}_{\ell+1} = \exp_{\bar{x}_\ell} \left(\frac{\alpha}{n} \sum_{i,j} \log_{\bar{x}_\ell}(x_{ij}) \right).$$

Of course, on $SO(3)$ we always lift into $\mathfrak{so}(3)$ and obtain the required tangent vectors by simple multiplication with the intrinsic mean \bar{R} or with the initial rotation R_0 , if desired. Here the update rule for the intrinsic mean of matrices R_{ij} becomes

$$\bar{R}_{\ell+1} = \bar{R}_\ell \exp \left(\frac{\alpha}{n} \sum_{i,j} \log(\bar{R}_\ell^T R_{ij}) \right).$$

4.4. Discussion of Accuracy. In this section we discuss the numerical accuracy of the nonlinear mappings implemented in Section 4. We start with the projections (9) for $SO(3)$ and (8) for S^2 , i.e., the accuracy of representing elements of these manifolds. Then we address the lift-and-project mappings $\exp \circ \log$ and $\exp \circ \text{lift}$ for $SO(3)$ and S^2 . For $SO(3)$, error statistics are based on 3 086 864 rotation matrices from the four examples in Section 5. For S^2 , we have 655 968 directors from the three S^2 examples in Section 5 plus 9 260 592 directors from the four $SO(3)$ examples.

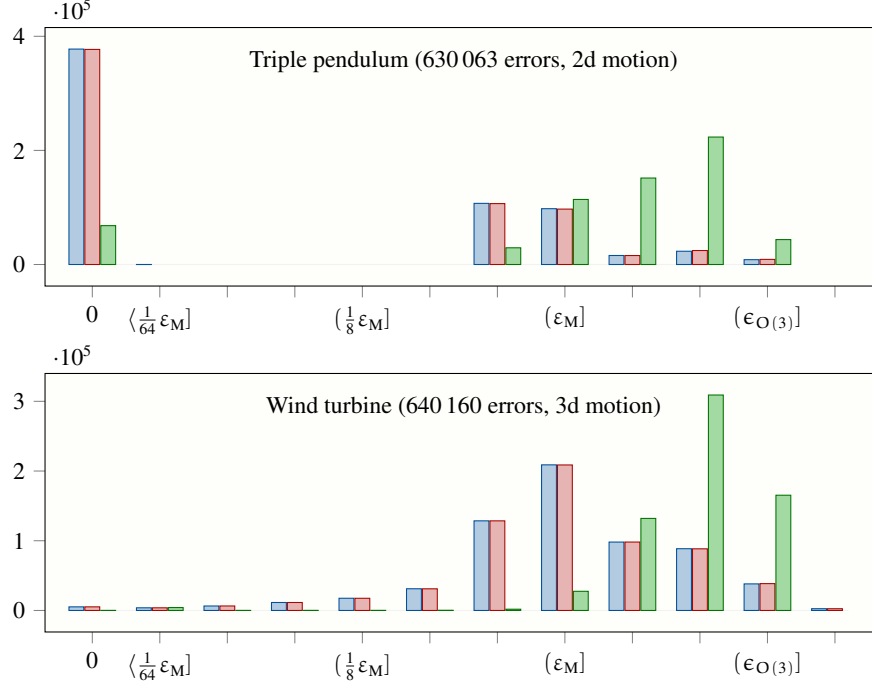


FIGURE 2. Bin counts of orthogonality error: R (green), $\exp(\log(R))$ (blue), $\exp(\text{lift}(R))$ (red). Error bins: $\langle x \rangle = (0, x]$, $(x] = (\frac{1}{2}x, x]$.

As already mentioned in Section 4.2, we can bound the orthogonality error on $SO(3)$, $e_{\perp}(R) = \|R^T R - I\|_{\max}$, by $\epsilon_{O(3)}$. If a rotation matrix R (from a numerical simulation, for instance) does not satisfy that bound, we replace it with its projection onto $SO(3)$ according to (9) using the LAPACK routine `dgesvd` [1]. Our numerical experiments show that this gives an accuracy of $\frac{7}{4}\epsilon_{O(3)}$ or better. Then, if necessary, a single Newton iteration for the equation $R^T R - I = 0$ reduces the error to at most $\epsilon_{O(3)}$.

For S^2 the situation is even better: when applying the projection (8), the *normalization error* $|1 - \|d\|_2|$ is zero in most cases (oscillating beam 79.2%, triple pendulum 77.2%, rubber rod 80.0%, wind turbine 64.2%, shell pendulum 63.1%, free flying plate 61.0%, tumbling cylinder 62.4%), and it lies in the range $[\frac{1}{2}\epsilon_M, 2\epsilon_M]$ in all other cases.

Orthogonality errors $e_{\perp}(R)$, $e_{\perp}(\exp(\log(R)))$ and $e_{\perp}(\exp(\text{lift}(R)))$ on $SO(3)$ are presented in Fig. 2 for the triple pendulum and the wind turbine. (The oscillating beam and the rubber rod perform 2d motions like the triple pendulum; they behave similarly and they are described in the text, but we omit visualizations.) Input matrices (R) are projected onto $SO(3)$ as just described if the initial error exceeds $\epsilon_{O(3)} = 8\epsilon_M$. This applies to 600 111 matrices for the wind turbine and none for the other cases. The maximal output error is $15\epsilon_M$ for the wind turbine and $\epsilon_{O(3)}$ or better in all other cases. The number of errors exceeding $\epsilon_{O(3)}$ is 2528 or 0.39% for $\exp \circ \log$ and 2492 or 0.38% for $\exp \circ \text{lift}$. As explained, a single Newton iteration will reduce all errors to at most $\epsilon_{O(3)}$ if desired. In summary, our results show that $\exp \circ \log$ and $\exp \circ \text{lift}$ map $SO(3)$ indeed to itself up to unavoidable numerical roundoff errors.

No visual or tabular presentations are given for the normality errors on S^2 since all of them are negligible.

The lift-and-project errors $\|\exp(\log(R)) - R\|_{\max}$ and $\|\exp(\text{lift}(R)) - R\|_{\max}$ for $SO(3)$ are shown in Fig. 3. These are crucial for PGA. We observe that the vast majority of errors are below $2^{12}\epsilon_M \approx 2e-12$, but a tiny fraction range up to almost $1e-4$. More detailed

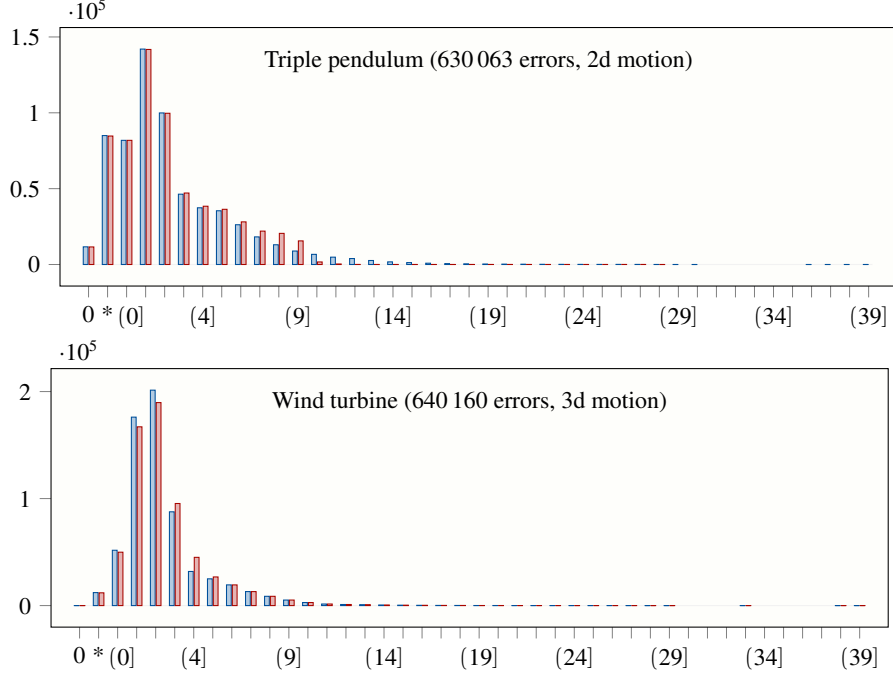


FIGURE 3. Bin counts of $SO(3)$ lift-and-project error: $\exp \circ \log$ (blue), $\exp \circ \text{lift}$ (red). Error bins: $*$ = $(0, \frac{1}{2} \varepsilon_M]$, (n) = $(2^{n-1} \varepsilon_M, 2^n \varepsilon_M]$.

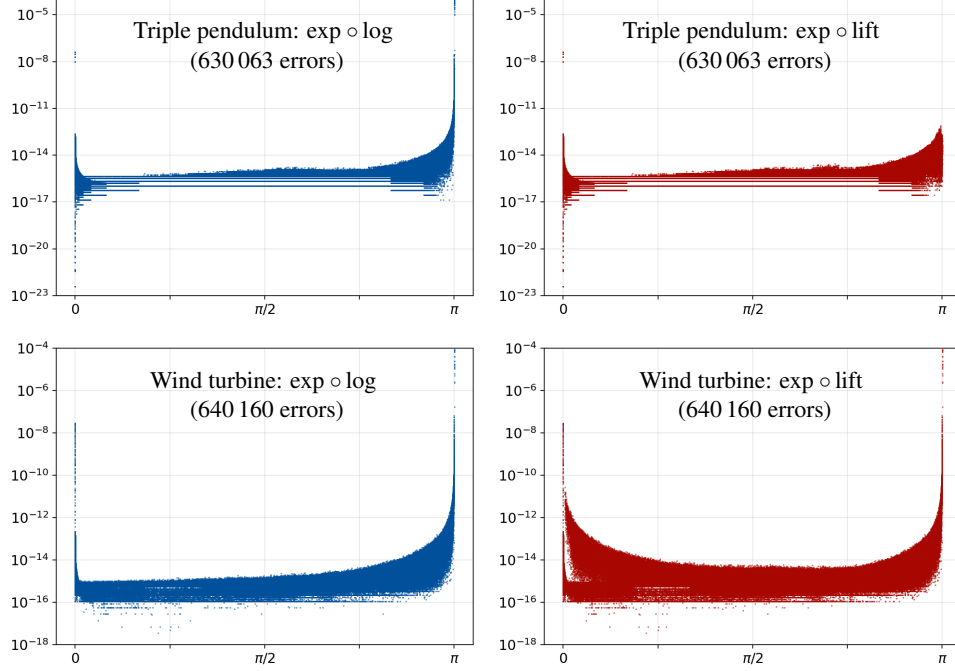
TABLE 1. Error statistics of $\exp \circ \log$ and $\exp \circ \text{lift}$ on $SO(3)$.

Dynamic system	error of $\exp \circ \log$			error of $\exp \circ \text{lift}$		
	maximal	large ($> 2^{12} \varepsilon_M$)		maximal	large ($> 2^{12} \varepsilon_M$)	
Oscillating beam	$3.9e-13$	0	0%	$2.3e-13$	0	0%
Triple pendulum	$8.5e-5$	8698	1.38%	$3.1e-8$	332	0.05%
Rubber rod	$9.5e-8$	59	1.13%	$1.5e-8$	11	0.21%
Wind turbine	$8.4e-5$	2762	0.43%	$8.4e-5$	2762	0.43%

information is provided in Table 1. A glance at the angular distribution of the lift-and-project errors in Fig. 4 reveals that, as expected, all these large errors occur at rotation angles close to zero and π : they are caused by the singularities of the logarithm map.

The lift-and-project errors for S^2 are illustrated in Fig. 5 for the three shell examples, and in Fig. 6 for the individual directors of the triple pendulum and the wind turbine. Again the majority of errors are below $2^{12} \varepsilon_M \approx 2e-12$ while the remaining ones are smaller than for $SO(3)$, with maximum at $5e-8$.

Excessive lift-and-project errors on $SO(3)$ can of course be reduced to $2^{12} \varepsilon_M$ or even to $\varepsilon_{O(3)}$ by performing certain critical operations with higher accuracy (128 bit quadruple precision might suffice). This should not even be overly expensive as it is only required close to the singularities. Moreover, arbitrary precision software such as the Multiprecision library of boost [27] might be used to save further cost by avoiding unnecessarily accurate computations. However, these issues are beyond the scope of this paper, and we need to point out that the current logarithm and lift maps for $SO(3)$ do not provide sufficient numerical precision for employing PGA-based model order reduction in dynamic simulations when matrices in the vicinity of the singularities occur.

FIGURE 4. Angular distributions of $SO(3)$ lift-and-project error.TABLE 2. Error statistics of $\exp_d \circ \log_d$ and $\exp_d \circ \text{lift}_d$ on S^2 .

Dynamic system	error of $\exp \circ \log$			error of $\exp \circ \text{lift}$		
	maximal	large ($> 2^{12} \epsilon_M$)		maximal	large ($> 2^{12} \epsilon_M$)	
Tumbling cylinder	4.0e-11	128	0.63%	4.0e-11	128	0.63%
Free-flying plate	3.6e-11	193	0.12%	3.6e-11	193	0.12%
Shell pendulum	1.7e-8	2363	0.49%	4.2e-8	2364	0.49%
Triple pendulum	1.7e-8	5070	0.27%	4.6e-8	5070	0.27%
Wind turbine	3.3e-8	84412	4.39%	4.9e-8	84667	4.41%

For S^2 the situation is definitely better, but with just below eight decimal digits in the worst case (error $4.9e-8$) it is probably still not good enough for PGA-based model order reduction in most situations. Thus, increasing the numerical precision of the logarithm and lift maps for S^2 will be a topic of further research as well.

5. COMPUTATIONAL EXAMPLES

5.1. Examples on $SO(3)$. To carry out our investigations on $SO(3)$, we select four examples: a swinging rubber rod, a free-oscillating cantilever beam, a flexible triple pendulum, and a horizontal-axis wind turbine. All four examples have been used for error statistics in Section 4.4, and we have earlier studied them in [11]. However, for the sake of brevity, the principal geodesic analysis on $SO(3)$ is carried out only for the triple pendulum and the wind turbine. In addition and due to the director-based formulation adopted in this work, the principal geodesic analysis on S^2 is also carried out for individual directors of the triple pendulum and wind turbine examples, whose results are presented in Section 5.2.

5.1.1. Rubber rod. This example considers a swinging rubber rod that is simply supported at one of its ends and subject only to the action of its own weight induced by gravity. Upon

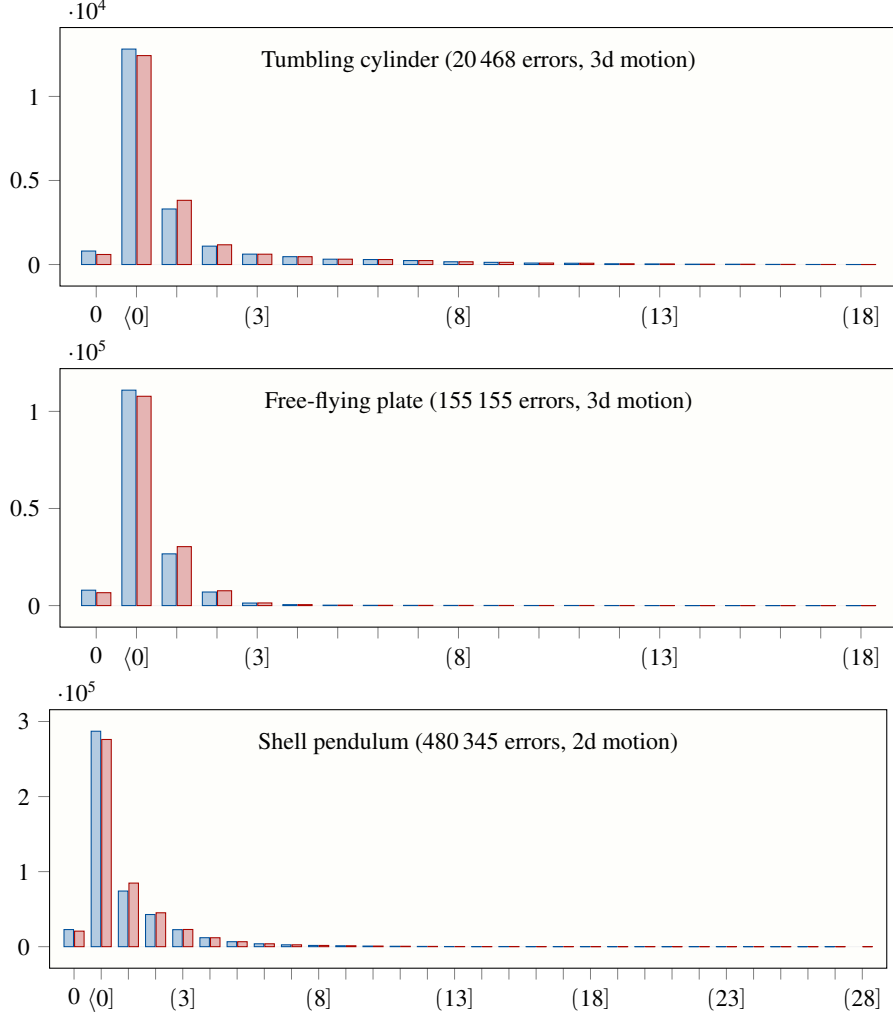


FIGURE 5. Bin counts of S^2 lift-and-project error: $\exp_d \circ \log_d$ (blue), $\exp_d \circ \text{lift}_d$ (red). Error bins: $\langle n \rangle = (0, 2^n \varepsilon_M]$, $(n) = (2^{n-1} \varepsilon_M, 2^n \varepsilon_M]$.

sudden release, the rod moves in a vertical plane exhibiting nonlinear kinematics. The geometrical and cross-sectional material properties of the rod are the following: length 1.0 m, circular cross-section with radius 0.005 m, elasticity modulus 5.0 MPa, Poisson's ratio 0.5, and mass density 1100 kg/m³. The acceleration of gravity is assumed to be 9.81 m/s². The rod is discretized into 20 finite elements, yielding 21 nodes. The time span simulated is 2.48 s and the time step is 0.01 s.

5.1.2. Oscillating beam. This example considers a cantilever beam with neutral straight configuration that is subject to the following simulation steps. In the first step, the beam is statically deformed under the action of a moment at the free end. The concentrated load applied is such that the cantilever beam reaches a deformed configuration corresponding to a semicircle. In the second step, the cantilever beam is dynamically released and oscillates exhibiting large displacements and large rotations in the plane defined by the semicircle. There is no gravity. The geometrical and material properties considered are the following: length 1.0 m, circular cross-section with radius 0.005 m, elasticity modulus

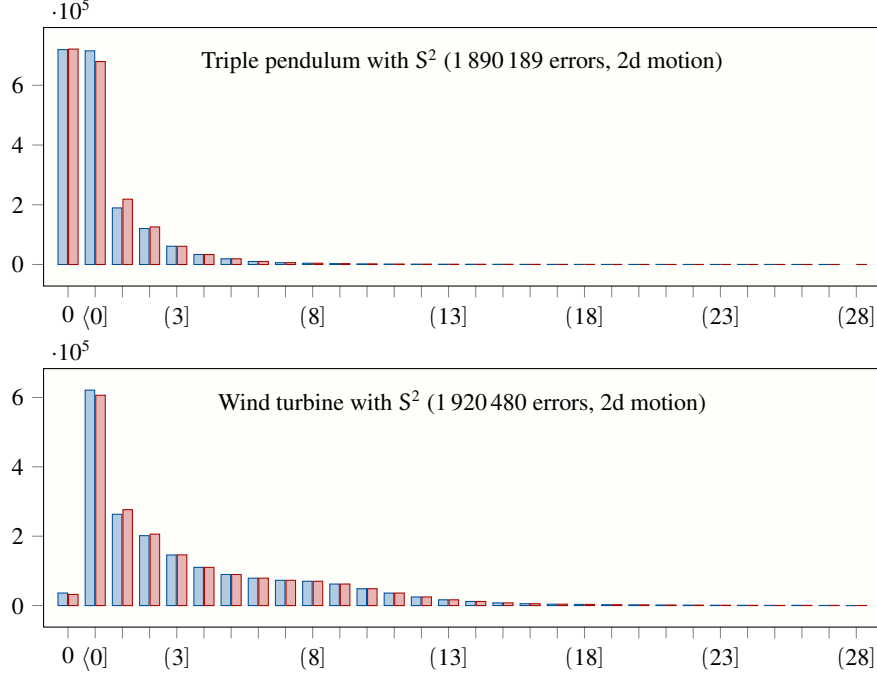


FIGURE 6. Bin counts of S^2 lift-and-project error for $SO(3)$ directors: $\exp_d \circ \log_d$ (blue), $\exp_d \circ \text{lift}_d$ (red). Error bins: $\langle n \rangle = (0, 2^n \varepsilon_M]$, $(n) = (2^{n-1} \varepsilon_M, 2^n \varepsilon_M]$.

1.273 GPa, shear modulus 0.637 GPa, and mass density 3183 kg/m^3 . The beam is uniformly discretized into 200 finite elements, yielding 201 nodes. The time span simulated is 10 s and the adopted time step is 0.001 s.

5.1.3. *Triple pendulum.* This example considers a pendulum that is built from three flexible straight links, identical in their properties, that are connected by means of spherical joints. The triple pendulum is simply supported at one of its ends and subject only to the action of its own weight induced by gravity. Upon sudden release, it moves in a vertical plane exhibiting nonlinear kinematics. The geometrical and cross-sectional material properties of each flexible link considered are the following: length 1.0 m, shear stiffness $5.0 \times 10^4 \text{ N/m}$, axial stiffness $1.0 \times 10^5 \text{ N/m}$, bending stiffness $6.25 \times 10^{-1} \text{ N/m}^2$, torsional stiffness 6.239 N/m^2 , mass density per unit length $2.5 \times 10^{-1} \text{ kg/m}$, inertia density per unit length $1.562 \times 10^{-6} \text{ kgm}$. The acceleration of gravity is assumed to be 9.81 m/s^2 . Each link is uniformly discretized into 20 finite elements, yielding 21 nodes and thus, a total of 63 nodes. The time span simulated is 10 s and the adopted time step is 0.001 s.

5.1.4. *Wind turbine.* This example considers the NREL 5 MW wind turbine, which comprises a tower, a nacelle, a hub, and three blades. The nacelle and hub are modeled as rigid bodies while the tower and blades are modeled as beams. The tower is clamped at the bottom and at the top, the nacelle is rigidly fixed to the tower. The blades are rigidly fixed to the hub, which is connected to the nacelle with a hinge, and thus only allowed to rotate about its symmetry axis. A force is applied in the middle of one blade. The force grows linearly between 0 and 5 s, reaching a maximum of $4.0 \times 10^5 \text{ N}$. After that, the force drops instantaneously to 0 N and remains so for the rest of the simulation. In contrast to the three prior examples, the motion developed by the wind turbine is truly three dimensional. Details on the geometrical and material properties are to be found in [17]. The tower is discretized into 10 elements while each blade is discretized into 48. The nacelle and the

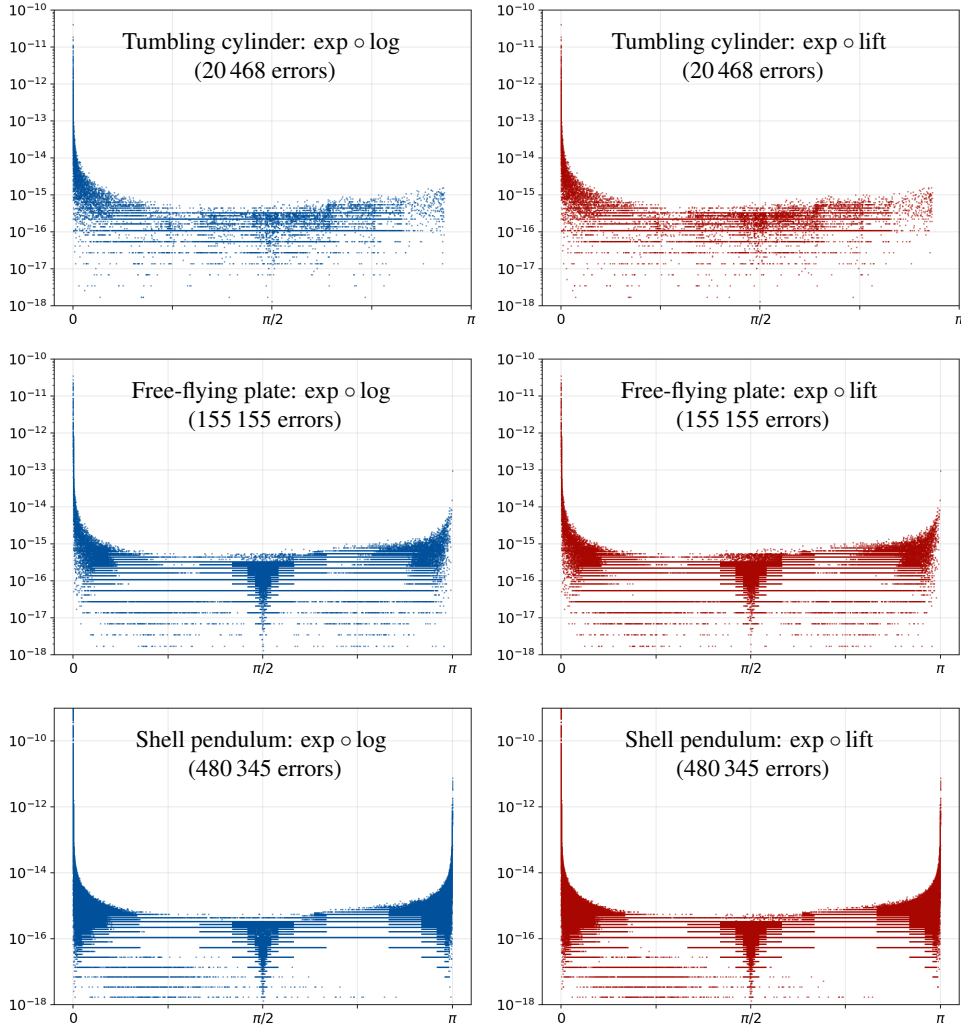


FIGURE 7. Angular distributions of S^2 lift-and-project error.

hub are represented by a single node each. The whole model accounts then for a total of 160 nodes. The time span simulated is 10 s and the adopted time step is 0.0025 s.

5.2. Examples on S^2 . To carry out our investigations on S^2 , we select three examples: a tumbling cylinder, a free-flying plate, and a shell pendulum. All three examples have been used as well for error statistics in Section 4.4. As already stated before, the principal geodesic analysis on S^2 is also carried out for individual directors of the triple pendulum and wind turbine examples corresponding to the set of examples on $SO(3)$.

5.2.1. Tumbling cylinder. This example considers a cylinder that is free to move in space, which has been already investigated many times in the past, see for instance [9] and references therein. A complex set of forces is applied at different locations of the cylinder. This set of forces is also subject to a time variation that grows linearly in the first half of the initial second and decreases linearly in its second half. After that, the forces remain zero for the rest of the simulation. The motion developed by the tumbling cylinder is truly three dimensional and exhibits large displacements and rotations. The geometrical and material properties of the cylinder are the following: radius 7.5 m, height 3.0 m, thickness 0.02 m, elastic modulus 0.2 GPa, Poisson's ratio 0.25, and mass density 1.0 kg/m^3 . The tumbling

TABLE 3. Overview of examples; the snapshot matrix Y has dimensions $m = \dim(\text{lift})$ and $n = \text{snapshots}$.

Dynamic system	motion	nodes	directors	dim(lift)	snapshots
Rubber rod	2d	21	63	63	249
Oscillating beam	2d	201	603	603	10001
Triple pendulum	2d	63	189	189	10001
Wind turbine	3d	160	480	480	4001
Tumbling cylinder	3d	68	68	116	301
Free-flying plate	3d	155	155	310	1001
Shell pendulum	3d (nearly 2d)	155	155	310	3099

cylinder is uniformly discretized into 48 elements along its perimeter and into 3 along its height. Thus it has 144 elements in total yielding 68 nodes, which means that the mesh has a seam modeled as continuous connection. The time span simulated is 3.0 s and the adopted time step is 0.01 s.

5.2.2. Free-flying plate. This example considers a plate that is free to move in space, which has been as well investigated before by Gebhardt and Rolfes [9] among others. A complex set forces is applied at different locations of the plate. This set of forces is also subject to a time variation that grows linearly between 0 and 0.002 s and decreases linearly between 0.002 and 0.004 s. After that, the forces remain zero for the rest of the simulation. The motion of the free-flying plate shows large displacements and rotations. Thus, its nonlinear kinematics is apparent. Moreover, the dynamical behavior is very rich in high-frequency content. The geometrical and material properties of the plate are the following: length 0.3 m, width 0.06 m, thickness 0.002 m, elastic modulus 206.0 GPa, Poisson's ratio 0.0, and mass density 7300.0 kg/m³. The free-flying plate is uniformly discretized into 30 elements along its length and into 4 along its width, i.e., 120 elements in total and yielding 155 nodes. The time span simulated is 0.1 s and the adopted time step is 0.0001 s.

5.2.3. Shell pendulum. This example considers a shell pendulum that is simply supported at one of its edges and subject only to the action of its own weight induced by gravity. Upon sudden release, the pendulum moves in space exhibiting nonlinear kinematics, but with the transversal plane as symmetry plane for the motion. The geometrical and material properties of the pendulum are the following: length 300.0 m, width 60 m, thickness 0.02 m, elastic modulus 2.06 MPa, shear modulus 1.03 MPa, and mass density 780 kg/m³. Some of the properties are intentionally chosen to be nonrealistic to the purpose only of triggering a complex dynamical behavior. The acceleration of gravity is assumed to be 9.81 kg/s². The shell pendulum is uniformly discretized into 30 elements along its length and into 4 along its width, i.e., 120 elements in total and yielding 155 nodes. The time span simulated is 3.098 s and the adopted time step is 0.001 s.

5.3. Computational Experiments. For each example described above the dynamic simulation yields several hundred to several thousand snapshots with several dozen to several hundred directors each; see Table 3. Each simulation is performed with a relative numerical accuracy between 1e−10 and 1e−8. The configuration manifold is either $(\mathbb{R}^3 \times \text{SO}(3))^{N_n}$ or $(\mathbb{R}^3 \times \text{S}^2)^{N_n}$ where N_n is the number of nodes, and we are only interested in the PGA on $\text{SO}(3)^{N_n}$ respectively $(\text{S}^2)^{N_n}$, with lifts in $\mathfrak{so}(3)^{N_n}$ respectively $\prod_{i=1}^{N_n} (\text{T}_{\text{d}_{i0}} \text{S}^2)^{N_n}$.

In order to evaluate the impact of lift-and-project errors on physical quantities associated with the resulting trajectories, we compute the total energy i) along the original sequence of snapshots; ii) along the lifted and projected sequence of snapshots with matrix Y (14); and iii), iv) along two sequences of snapshots obtained by projecting truncated singular value decompositions Y_p after the lifting (15), (16): a “good” one with a larger rank p , and

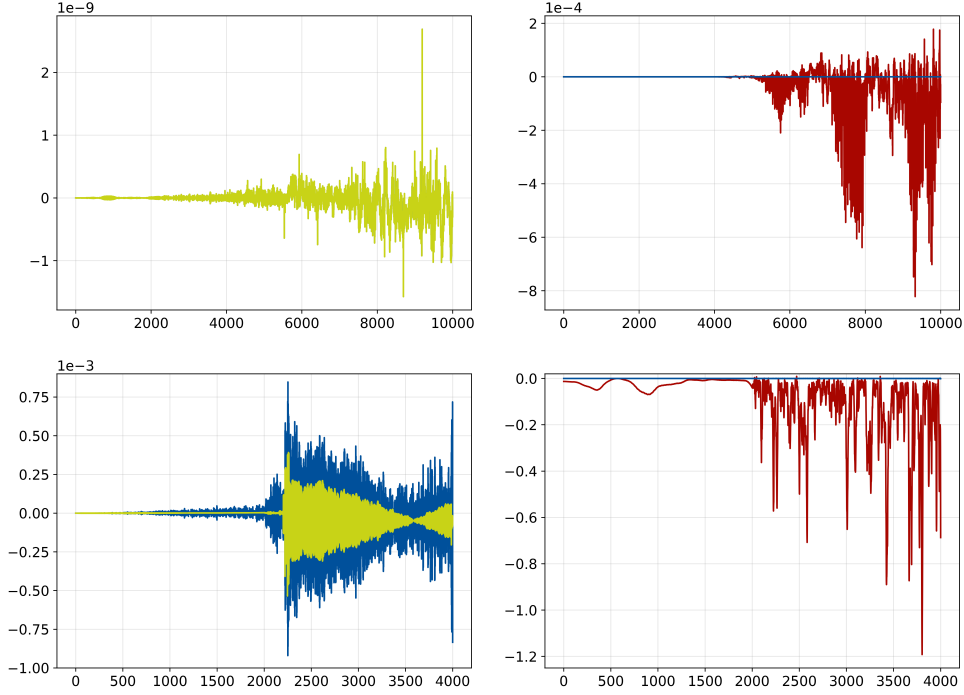


FIGURE 8. $SO(3)$: relative difference of original vs. $\exp \circ$ lift energy. Triple pendulum (top left: Y green, Y_{63} blue; right: Y_{63} blue, Y_{62} red), wind turbine (bottom left: Y red, Y_{345} blue; right: Y_{345} blue, Y_{35} red).

a “poor” one with a smaller rank p . Relative differences of each lift-and-project energy to the original total energy (which is invariant over time) are presented in Fig. 8 for the three $SO(3)$ examples and in Fig. 9 for the two S^2 examples. The values of the reference energy (denominators) of the relative differences are as follows. For the triple pendulum (10.9 J) and the shell pendulum (0.0406 J), the reference energy is the difference between initial and minimal potential energy reached during the simulation, i.e., the maximal sum of kinetic energy plus elastic energy. For the wind turbine (2.62×10^5 J), the tumbling cylinder (445 J), and the free-flying plate (246 J), it is the energy added to each system by applying the respective initial forces.

For the triple pendulum we see in Fig. 8 (top left) that the lift-and-project map without truncation (green) and with truncation at $p = 63$ (blue, invisible) give visually identical results, with a maximal error of about $3e-8$ in conserving the original energy. This is because we have a planar rotation that is exactly reproduced by the selected 63 (out of 189) SVD modes: the relative truncation error is numerically zero at $\sigma_{63}/\sigma_1 = 2\varepsilon_M \approx 4e-16$ and $\|Y - Y_{63}\|_{\max}/\sigma_1 \approx 8e-17$. With just one mode less, at $p = 62$, the energy error grows drastically to a maximum of about $9e-3$ (red curve in top right plot). Here we have truncation errors $\sigma_{62}/\sigma_1 \approx 1e-4$ and $\|Y - Y_{62}\|_{\max}/\sigma_1 \approx 2e-6$. As a function of time, all errors start out very small and start growing significantly only after about 5000 time steps.

The 3d motion of the wind turbine exhibits significantly larger energy errors (Fig. 8, bottom left). The maximal error without truncation is roughly $5e-4$ (green curve), and it doubles approximately with a good approximation by 345 (out of 480) SVD modes (blue curve). Here the truncation errors are $\sigma_{345}/\sigma_1 \approx 1e-8$ and $\|Y - Y_{345}\|_{\max}/\sigma_1 \approx 2e-9$. The poor approximation at $p = 35$ has truncation errors similar to the poor approximation of the triple pendulum, $\sigma_{35}/\sigma_1 \approx 4e-5$ and $\|Y - Y_{35}\|_{\max}/\sigma_1 \approx 2e-6$. This gives very large energy errors up to 1.2 or 120% (red curve, bottom right). The temporal behavior is similar to the triple pendulum, with rather small errors during the first half of the simulation.

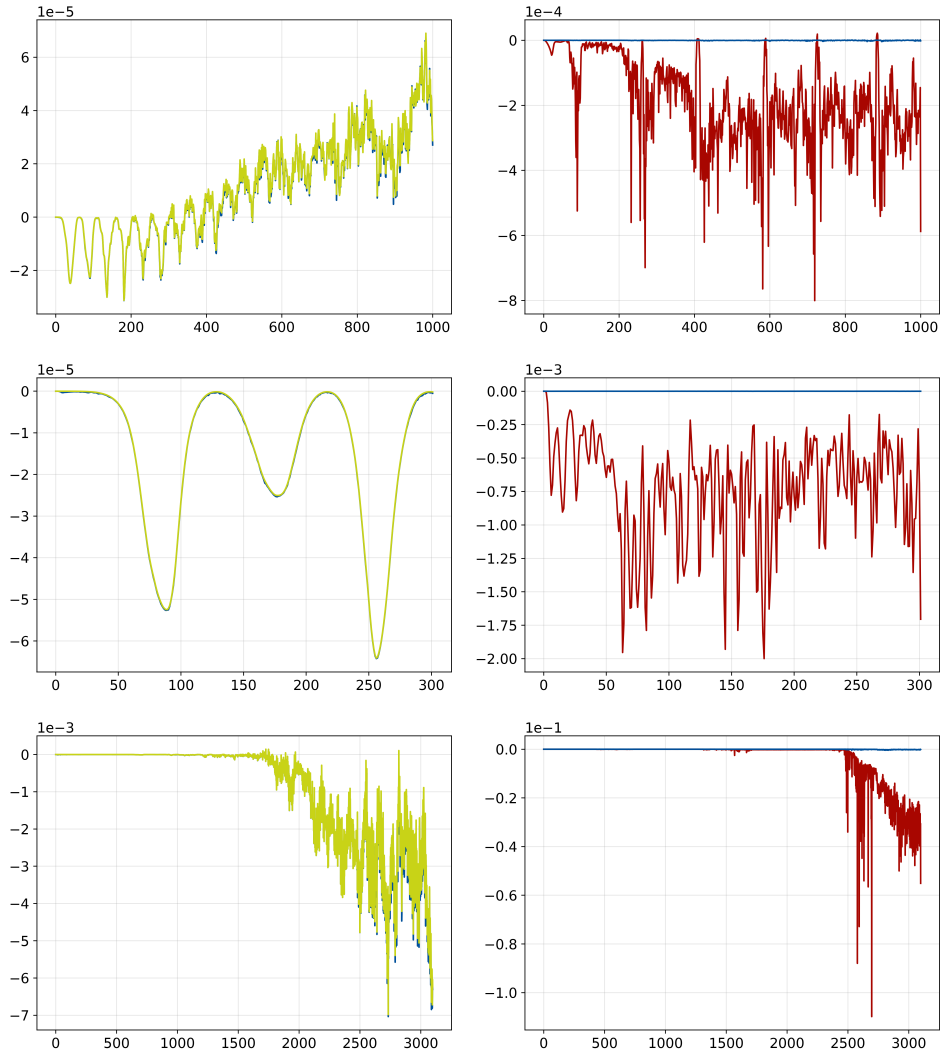


FIGURE 9. S^2 : relative difference of original vs. $\exp \circ$ lift energy. Tumbling cylinder (top left: Y green, Y_{84} blue; right: Y_{84} blue, Y_{47} red) free-flying plate (middle left: Y green, Y_{295} blue; right: Y_{295} blue, Y_{222} red), shell pendulum (bottom left: Y green, Y_{239} blue; right: Y_{239} blue, Y_{133} red).

For the shell pendulum in Fig. 9 (bottom), results are in part comparable to the triple pendulum: the lift-and-project energy error without truncation (green) and with a good approximation at $p = 239$ (blue) are visually almost identical, both with a maximum of roughly $7e-3$ and with very small values for the first half of the simulation. Here the truncation error is $\sigma_{239}/\sigma_1 \approx 7e-5$. The poor approximation, however, with only 133 (out of 310) modes and a truncation error of $\sigma_{133}/\sigma_1 \approx 1e-3$, yields comparatively large energy errors up to 0.11, i.e., 11%. On the other hand, these large errors develop later on during the simulated time span.

The energy errors of the free-flying plate and of the tumbling cylinder in Fig. 9 (top and middle) behave similarly, except that in both cases the errors start developing early on during the simulation while accuracies of the lift and of the selected approximations are higher than for the shell pendulum. The truncation errors for the free-flying plate are

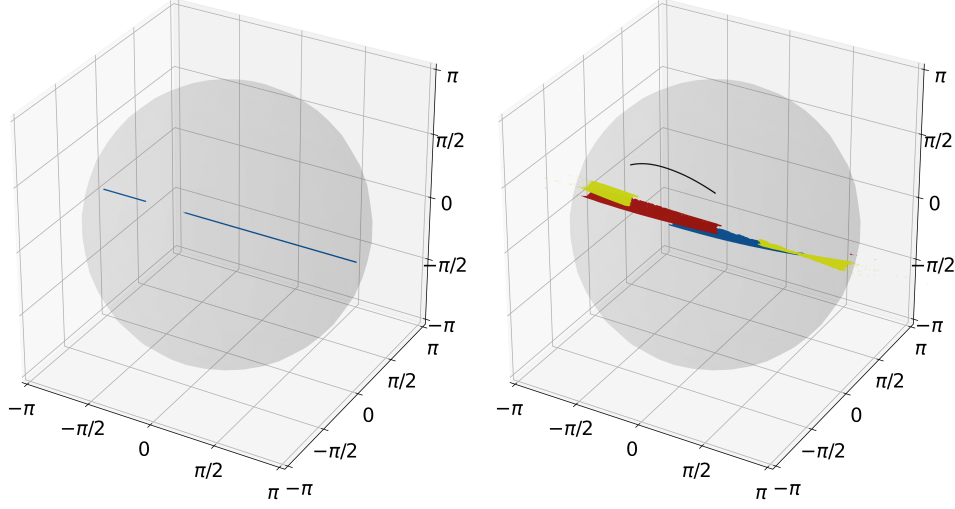


FIGURE 10. Distribution of logarithms of rotations in Lie algebra $\mathfrak{so}(3)$: triple pendulum (left), wind turbine (right: tower black, blades colored).

$\sigma_1/\sigma_{295} \approx 1e-5$ (good approximation) and $\sigma_1/\sigma_{222} \approx 1e-4$ (poor approximation). For the tumbling cylinder they are $\sigma_1/\sigma_{84} \approx 8e-7$ (good approximation) and $\sigma_1/\sigma_{47} \approx 5e-5$ (poor approximation).

5.4. Discrete Trajectories and Lifts. Finally we illustrate some properties of the logarithms and lifts for selected discrete trajectories of the examples. Here we call the rotation matrices of the finite element nodes *orientations* to distinguish them from the rotations that the physical bodies perform.

In Fig. 10 we see the logarithms of all $630\,063 = 63 \times 10001$ orientations of the triple pendulum (left) and all $640\,160 = 160 \times 4001$ orientations of the wind turbine (right), which lie in the closed ball $\bar{B}_\pi \subset \mathfrak{so}(3)$ (indicated in grey). Because of the planar motion of the triple pendulum, all logarithms lie in a one-dimensional subspace of $\mathfrak{so}(3)$, i.e., on a straight line, which corresponds to the fixed direction that the axes of rotation of all nodes share. This is immediately apparent from the picture. For the wind turbine, it is clearly visible that the logarithms of all trajectories of blades' orientations (colored) lie close to the same straight line but with notable differences: the blades' trajectories exhibit slight deviations from strictly planar rotation, so that a true 3d motion results. The logarithms of the tower orientations (black) show even larger deviations from a planar motion.

For the S^2 examples, Fig. 11 (left) presents the distributions of all individual directors on the sphere: $20\,468 = 68 \times 301$ for the tumbling cylinder, $155\,155 = 155 \times 1001$ for the free-flying plate, and $480\,345 = 155 \times 3099$ for the shell pendulum. Here we observe quite different behavior: the tumbling cylinder has 68 clearly distinguishable trajectories of tightly spaced directors, the free-flying plate has 155 trajectories of widely spaced directors that cover the entire sphere almost uniformly, and the shell pendulum has again 155 trajectories of widely spaced directors that are, however, concentrated along a great circle of the sphere.

The corresponding logarithms in the closed disk $\bar{D}_\pi \subset T_{(0,0,1)}S^2$ (indicated in grey) are displayed on the right of Fig. 11. Notice that the lifted discrete trajectory of each finite element node $i \in \{1, \dots, N_n\}$ has its own tangent space, $T_d S^2$ with $d = d_{i0}$. To illustrate all these lifted trajectories simultaneously, we rotate each tangent space $T_d S^2$

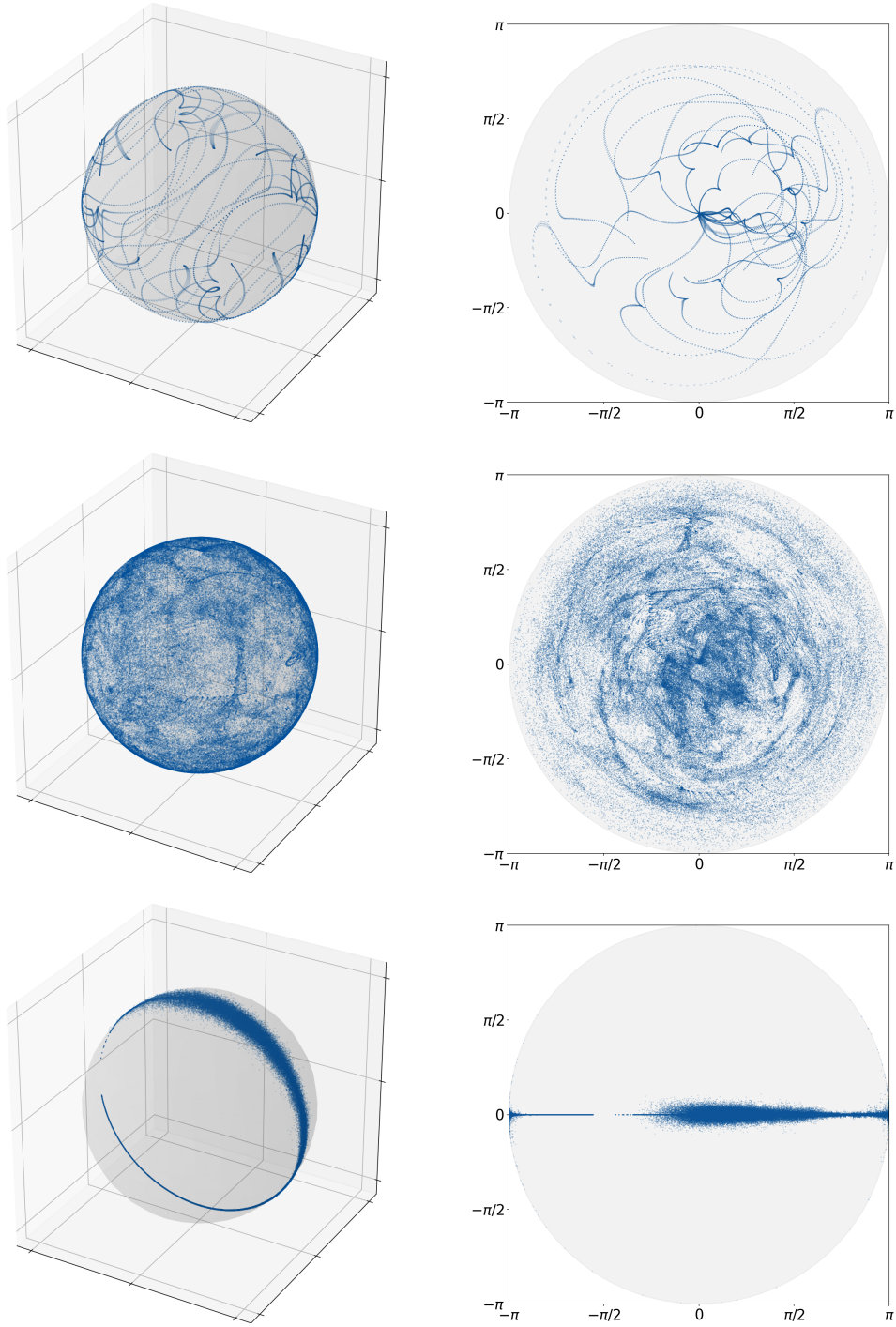


FIGURE 11. Distribution of directors on sphere S^2 (left) and of their logarithms in tangent space $T_{(0,0,1)}S^2$ (right): tumbling cylinder (top), free-flying plate (middle), shell pendulum (bottom).

into the tangent space $T_{(0,0,1)}S^2$ at the north pole via

$$\mathbf{R}(\mathbf{d}) := \begin{bmatrix} 1 & 0 & -d_1 \\ 0 & 1 & -d_2 \\ d_1 & d_2 & 1 \end{bmatrix} - q(\mathbf{d}) \begin{bmatrix} d_1^2 & d_1 d_2 & 0 \\ d_1 d_2 & d_2^2 & 0 \\ 0 & 0 & d_1^2 + d_2^2 \end{bmatrix}, \quad q(\mathbf{d}) := \frac{1}{1 + d_3}.$$

For a vector $\mathbf{v} \in T_{\mathbf{d}}S^2$ we exploit the orthogonality relation $\langle \mathbf{d}, \mathbf{v} \rangle = 0$ to obtain

$$\mathbf{R}(\mathbf{d})\mathbf{v} = \begin{pmatrix} v_1 - d_1 v_3 - q(\mathbf{d})(v_1 d_1^2 + v_2 d_1 d_2) \\ v_2 - d_2 v_3 - q(\mathbf{d})(v_1 d_1 d_2 + v_2 d_2^2) \\ 0 \end{pmatrix} = \begin{pmatrix} v_1 - d_1 q(\mathbf{d})v_3 \\ v_2 - d_2 q(\mathbf{d})v_3 \\ 0 \end{pmatrix}.$$

(Here the coefficient map $q: S^2 \setminus \{(0, 0, -1)\} \rightarrow \mathbb{R}$ and consequently the rotation map $\mathbf{R}: S^2 \setminus \{(0, 0, -1)\} \rightarrow \text{SO}(3)$ are undefined at the south pole $\mathbf{d} = (0, 0, -1)$.) Again the different behavior of the three dynamical systems is immediately apparent from the pictures: the logarithms of the directors of the tumbling cylinder form clearly distinguishable trajectories, the ones of the free-flying plate cover the disk \bar{D}_π almost uniformly, and the logarithms of the shell pendulum are concentrated along a straight line, which indicates once more near-planar motion with slight deviations.

Analogous distributions for the individual directors d_i of the wind turbine's orientations are shown in Fig. 12, again with all tangent spaces rotated into $T_{(0,0,1)}S^2$. Here it is harder to infer the type of motion from the pictures. However, except for the tower (black), which clearly exhibits some true 3d motion, the distributions of directors on the sphere (left) clearly show that d_1 performs small movements around a nearly fixed director for each node of each blade (colored); this nearly fixed director is the horizontal axis of rotation. Consequently, the directors d_2 and d_3 of all blades' nodes move close to great circles. Only the first logarithm plot, associated with d_1 , appears to convey a clear situation. However, due to the rotation of all tangent spaces into $T_{(0,0,1)}S^2$, significant information gets lost so that these pictures do not permit a well-founded interpretation.

Finally we present in Fig. 13 a visualization of the lifted trajectory of the wind turbine. The ball \bar{B}_π is again indicated in grey so that the presence of branch switchings for the logarithm map is immediately apparent. This illustration also shows that the lifts of all finite element nodes of each blade cover a connected area, which is again concentrated along a straight line. In contrast, the green-yellowish blade appears to cover two disconnected areas in Fig. 10.

6. CONCLUSIONS

In this article, we presented new computational realizations of PGA for the unit sphere S^2 and the special orthogonal group $\text{SO}(3)$. In addition, we carefully considered the consequences that singularities have on the numerical accuracy of the proposed algorithms to construct long-time smooth lifts across branches of the respective logarithmic maps. Finally, we applied our PGA realization to investigate several interesting mechanical systems. Even provided that our results are encouraging, especially regarding the potential for this approach to be used in the derivation of structure-preserving reduced-order models, there are still many open issues that will be considered in the sequel.

Among those open issues we identify as the most urgent ones: *i*) applying higher accuracy for lifting close to singularities, which could be addressed by considering multiprecision arithmetic; *ii*) employing periodic, but discontinuous lifts instead of continuous ones, but across branches; *iii*) carrying out PGA on the special Euclidean group $\text{SE}(3)$ instead of carrying out PCA on \mathbb{R}^3 and PGA on $\text{SO}(3)$ separately. Recall that the Lie groups $\text{SE}(3)$ and $\text{SO}(3) \times \mathbb{R}^3$ are diffeomorphic as manifolds, but not isomorphic as groups; *iv*) further investigating degradation of mechanical invariants such as momenta and energy upon truncation; and finally, *v*) deriving structure-preserving reduced-order models based on PGA.

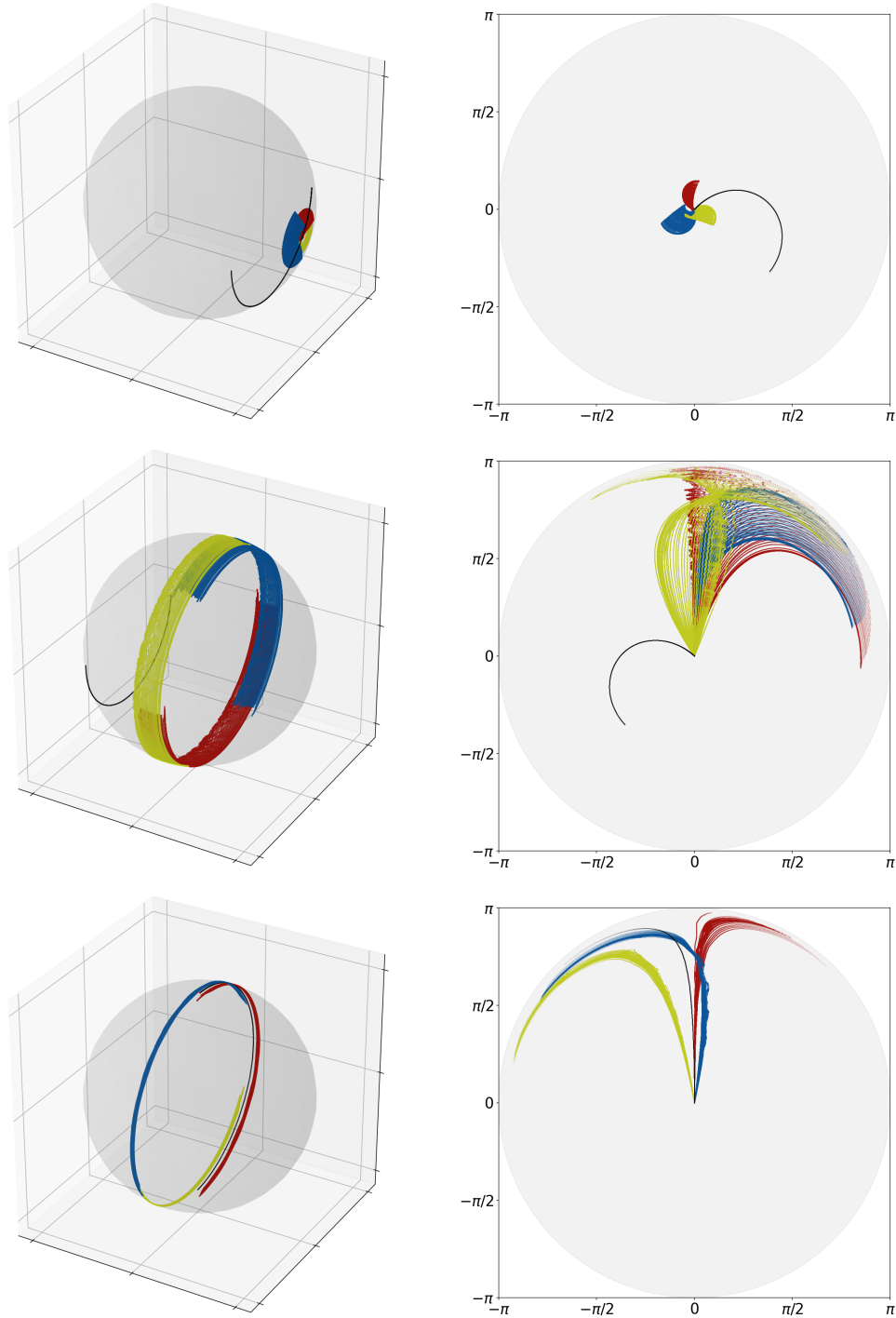


FIGURE 12. Rotations $R = [d_1 \ d_2 \ d_3] \in S^2 \times S^2 \times S^2$ for wind turbine (tower black, blades colored): distribution of directors on sphere S^2 (left) and of their logarithms in tangent space $T_{(0,0,1)}S^2$; d_1 to d_3 (top to bottom).

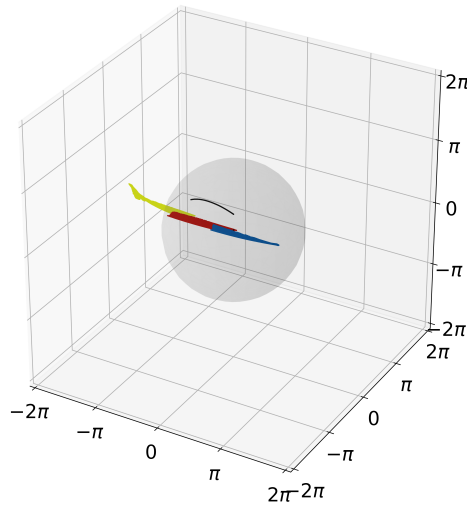


FIGURE 13. Lift with branch switching of wind turbine in $\mathfrak{so}(3)$.

DATA AVAILABILITY

The data supporting this manuscript can be provided upon reasonable request.

CONFLICT OF INTEREST STATEMENT

The authors declare that they have no known competing financial interests or personal relationships that could have appeared to influence the work reported in this manuscript.

ACKNOWLEDGEMENTS

The second and third authors are funded by the Deutsche Forschungsgemeinschaft (DFG, German Research Foundation) – SFB1463 – 434502799.

REFERENCES

- [1] E. ANDERSON, Z. BAI, C. BISCHOF, J. DEMMEL, J. DONGARRA, J. DU CROZ, A. GREENBAUM, S. HAMMARLING, A. MCKENNEY, S. OSTROUCHOV, AND D. SORENSEN, *LAPACK Users' Guide*, SIAM, Philadelphia, PA, 1992. <http://www.netlib.org/lapack>.
- [2] E. CAZELLES, V. SEGUY, J. BIGOT, M. CUTURI, AND N. PAPADAKIS, *Geodesic PCA versus Log-PCA of histograms in the Wasserstein space*, SIAM Journal on Scientific Computing, 40 (2018), pp. B429–B456.
- [3] R. CHAKRABORTY, D. SEO, AND B. VEMURI, *An efficient exact-PGA algorithm for constant curvature manifolds*, in Proceedings of the IEEE Conference on Computer Vision and Pattern Recognition, 2016, pp. 3976–3984.
- [4] C. CURRY, S. MARSLAND, AND R. MCLACHLAN, *Principal symmetric space analysis*, Journal of Computational Dynamics, 6 (2019), pp. 251–276.
- [5] P. FLETCHER, C. LU, AND S. JOSHI, *Statistics of shape via principal geodesic analysis on Lie groups*, in 2003 IEEE Computer Society Conference on Computer Vision and Pattern Recognition, 2003. Proceedings, vol. 1, 2003, pp. I–I.
- [6] P. FLETCHER, C. LU, S. M. PIZER, AND S. JOSHI, *Principal geodesic analysis for the study of nonlinear statistics of shape*, IEEE Transactions on Medical Imaging, 23 (2004), pp. 995–1005.
- [7] H. FOTOUHI AND M. GOLALIZADEH, *Exploring the variability of DNA molecules via principal geodesic analysis on the shape space*, Journal of Applied Statistics, 39 (2012), pp. 2199–2207.
- [8] C. GEBHARDT, B. HOFMEISTER, C. HENTE, AND R. ROLFES, *Nonlinear dynamics of slender structures: a new object-oriented framework*, Computational Mechanics, - (2018), pp. 1–34.
- [9] C. GEBHARDT AND R. ROLFES, *On the nonlinear dynamics of shell structures: combining a mixed finite element formulation and a robust integration scheme*, Thin-Walled Structures, 118 (2017), pp. 56–72.
- [10] C. GEBHARDT, I. ROMERO, AND R. ROLFES, *A new conservative/dissipative time integration scheme for nonlinear mechanical systems*, Computational Mechanics, 65 (2020), pp. 405–427.

- [11] C. GEBHARDT, M. C. STEINBACH, AND R. ROLFES, *Understanding the nonlinear dynamics of beam structures: a principal geodesic analysis approach*, Thin-Walled Structures, 140 (2019), pp. 357–372.
- [12] W. B. HEARD, *Rigid Body Mechanics: Mathematics, Physics and Applications*, Wiley, 2006.
- [13] B. HEEREN, C. ZHANG, M. RUMPF, AND W. SMITH, *Principal geodesic analysis in the space of discrete shells*, Computer Graphics Forum, 37 (2018), pp. 173–184.
- [14] M. HERNANDEZ, *Efficient momentum conservation constrained PDE-LDDMM with Gauss–Newton–Krylov optimization, semi-Lagrangian Runge–Kutta solvers, and the band-limited parameterization*, Journal of Computational Science, 55 (2021), p. 101470.
- [15] S. HUCKEMANN, T. HOTZ, AND A. MUNK, *Intrinsic shape analysis: geodesic PCA for Riemannian manifolds modulo isometric Lie group actions*, Statistica Sinica, 20 (2010), pp. 1–58.
- [16] I. JOLLIFFE, *Principal Component Analysis*, Springer Series in Statistics, Springer New York, 1986.
- [17] J. JONKMAN, S. BUTTERFIELD, W. MUSIAL, AND G. SCOTT, *Definition of a 5-MW reference wind turbine for offshore system development*, tech. rep., National Renewable Energy Laboratory (NREL), Golden, CO., 2009.
- [18] W. KLINGENBERG, *Riemannian Geometry*, vol. 1 of studies in mathematics, De Gruyter, Berlin, 1982.
- [19] D. LAZAR AND L. LIN, *Scale and curvature effects in principal geodesic analysis*, Journal of Multivariate Analysis, 153 (2017), pp. 64–82.
- [20] J. LEE AND M. VERLEYSSEN, *Nonlinear Dimensionality Reduction*, Springer Series in Statistics, Springer New York, 2007.
- [21] P. REN, F. AZIZ, L. HAN, E. XU, R. C. WILSON, AND E. R. HANCOCK, *Geometricity and Embedding*, Springer London, 2013, pp. 121–155.
- [22] S. SAID, N. COURTY, N. LE BIHAN, AND S. SANGWINE, *Exact principal geodesic analysis for data on $SO(3)$* , in 2007 15th European Signal Processing Conference, 2007, pp. 1701–1705.
- [23] H. SALEHIAN, D. VAILLANCOURT, AND B. VEMURI, *iPGA: incremental principal geodesic analysis with applications to movement disorder classification*, in International Conference on Medical Image Computing and Computer-Assisted Intervention, vol. 17, 2014, pp. 765–772.
- [24] F. SITTEL, T. FILK, AND G. STOCK, *Principal component analysis on a torus: theory and application to protein dynamics*, The Journal of Chemical Physics, 147 (2017), p. 244101.
- [25] S. SOMMER, F. LAUZE, AND M. NIELSEN, *Optimization over geodesics for exact principal geodesic analysis*, Advances in Computational Mathematics, 40 (2014), pp. 283–313.
- [26] M. TOURNIER, X. WU, N. COURTY, E. ARNAUD, AND L. REVÉRET, *Motion compression using principal geodesics analysis*, Computer Graphics Forum, 28 (2009), pp. 355–364.
- [27] *Boost C++ Libraries*. <http://www.boost.org/>, 1998-2022.

CRISTIAN G. GEBHARDT, UNIVERSITY OF BERGEN, GEOPHYSICAL INSTITUTE AND BERGEN OFFSHORE WIND CENTRE (BOW), ALLÉGATEN 70, 5007 BERGEN, NORWAY

Email address: cristian.gebhardt@uib.no

URL: uib.no/en/persons/Cristian.Guillermo.Gebhardt

JENNY SCHUBERT, LEIBNIZ UNIVERSITÄT HANNOVER, INSTITUTE OF APPLIED MATHEMATICS, WELFENGARTEN 1, 30167 HANNOVER, GERMANY

Email address: schubert@ifam.uni-hannover.de

URL: ifam.uni-hannover.de/schubert

MARC C. STEINBACH, LEIBNIZ UNIVERSITÄT HANNOVER, INSTITUTE OF APPLIED MATHEMATICS, WELFENGARTEN 1, 30167 HANNOVER, GERMANY

Email address: mcs@ifam.uni-hannover.de

URL: ifam.uni-hannover.de/mcs